THE ASTROPHYSICAL JOURNAL, 509:324–349, 1998 December 10
© 1998. The American Astronomical Society. All rights reserved. Printed in U.S.A.

HIGH-RESOLUTION FAR-INFRARED STUDIES OF INTERMEDIATE-MASS PRE–MAIN-SEQUENCE OBJECTS

JAMES DI FRANCESCO,[1] NEAL J. EVANS II, AND PAUL M. HARVEY
University of Texas at Austin, Austin, TX 78712-1083; jdifran@cfa.harvard.edu, nje@astro.as.utexas.edu, pmh@astro.as.utexas.edu

LEE G. MUNDY
University of Maryland, College Park, MD 20742; lgm@astro.umd.edu

AND

HAROLD M. BUTNER
Steward Observatory, University of Arizona, Tucson, AZ 85721; hbutner@as.arizona.edu

Received 1998 March 19; accepted 1998 July 20

ABSTRACT

We have obtained high-resolution far-infrared maps of nine regions with 10 Herbig Ae/Be stars (intermediate-mass pre–main-sequence stars). Similar maps were obtained for 10 embedded *IRAS* sources with $S_\nu(100\ \mu\text{m}) > S_\nu(60\ \mu\text{m})$ and $L \sim 200\ L_\odot$, which are possible evolutionary precursors of Herbig Ae/Be stars. Single far-infrared sources were found in most maps. The embedded sources have positions in agreement with those of the *IRAS* PSC, but some of the Herbig Ae/Be stars are offset significantly from the position of peak far-infrared emission. For all objects where it was possible to obtain 100 μm flux densities, they are consistent with those observed by *IRAS*, but derived 50 μm flux densities are larger than expected. The far-infrared maps reveal that objects in at least 17 of 19 emission regions are significantly extended at the 30″–40″ resolution of the Kuiper Airborne Observatory at 100 μm. Only sources associated with AB Aur and possibly *IRAS* 05338−0624 have unresolved far-infrared emission. Detailed analyses of the flux densities and positions from our maps suggest the far-infrared emission in regions with Herbig Ae/Be stars may not immediately surround these stars in all cases. Instead, far-infrared emission from these objects may originate from dust heated externally by the Herbig stars, or from dust heated internally by other sources. For other objects arguably surrounded by far-infrared emission, the Herbig stars or embedded *IRAS* objects have similar mean deconvolved sizes (i.e., 0.10–0.15 pc), but possibly have different mean deconvolved shapes (i.e., aspect ratios). Thus, far-infrared emission here may originate from flattened dust envelopes; the appearance of a far-infrared object as either a Herbig Ae/Be star or an embedded *IRAS* source may be merely a matter of viewing orientation.

Subject headings: infrared: stars — stars: pre–main-sequence

1. INTRODUCTION

Protostellar objects form deep within molecular clouds as the result of the gravitational collapse of dense core material. Most studies of this process have focused on low-mass objects (i.e., $M_* < 2\ M_\odot$), for which a standard model has been developed (see Shu et al. 1993 for a general review). In this model, collapse begins within an isothermal core having a steep density distribution [$n(r) \propto r^{-2.0}$] and proceeds from the inside out. However, it is uncertain if the formation of high-mass stars adheres to this model. For example, different physical conditions within some dense cores could promote the formation of higher mass stars over lower mass stars. Fuller & Myers (1992) (see also Myers & Fuller 1992) proposed that some envelopes also may be supported by nonthermal, turbulent processes, which allows initial core density distributions to be shallower than $n(r) \propto r^{-2.0}$, and such processes could be more important in the formation of massive stars (see, e.g., Myers, Ladd, & Fuller 1991). Evidence for a link between stellar mass and the initial distribution of core material may be retained within protostellar envelopes whose structures reflect the physical conditions of collapse.

Pre–main-sequence objects of intermediate mass (i.e., 2–10 $M_\odot$) provide excellent opportunities to determine the upper mass limit for which the inside-out collapse picture is relevant, and to investigate links between initial physical conditions and stellar mass. The environments surrounding these objects are less disrupted than those of still higher mass stars, but they are luminous enough to generate sufficient far-infrared emission to probe envelope structure. Typically, spectral energy distributions (SEDs) alone, including far-infrared flux densities, have been used to constrain models of the circumstellar environment of these objects, but this method leaves open the question of whether the emission at a given wavelength arises from a disk or from a much more extended envelope. Di Francesco et al. (1994) demonstrated that far-infrared continuum images can distinguish between disks and envelopes. For example, disks of size ∼100 AU should appear unresolved to the Kuiper Airborne Observatory (KAO) at far-infrared wavelengths, where its 30″–40″ beam equals 4200–5600 AU on the sky at the distance of the nearest young objects in Taurus. If the emission is extended, it arises in the envelopes, and the extent of the emission can provide an independent constraint to models of collapse.

Examples of intermediate-mass objects include the Herbig Ae/Be stars: young stellar objects that are the intermediate-mass counterparts to the T Tauri stars (Herbig 1960; Thé, de Winter, & Pérez 1994). High-resolution far-infrared observations from the KAO have been used already to constrain models of the envelopes of these stars. For example, Natta et al. (1993) obtained one-dimensional (1D) 100 μm cuts across regions containing

[1] Currently at Harvard-Smithsonian Center for Astrophysics, 60 Garden Street, MS42, Cambridge, MA 02138.

seven Herbig Ae/Be stars (or similar objects) and found five to be extended at 30″–40″ spatial resolution. The observed sizes and SEDs of these five sources were reproduced using spherical envelope models similar to those used by Butner et al. (1991) to characterize the envelope of the low-mass young stellar object L1551 IRS 5. Although two sources required density distributions typical of early low-mass collapse [i.e., $n(r) \propto r^{-2.0}$], the other three sources required distributions much shallower than suggested by the standard model [i.e., $n(r) \propto r^{-0.5}$; see also Natta et al. 1992 and Butner & Natta 1995 for models of the envelope of Herbig Ae/Be star LkHα 198]. Di Francesco et al. (1994) obtained 1D far-infrared cuts across six regions containing other Herbig Ae/Be stars with more modest infrared excesses than those studied by Natta et al. (1992). In this study, five of six objects were also extended at 100 μm, which indicates that the far-infrared emission comes from envelopes rather than disks.

The visible Herbig Ae/Be stars are generally assumed to be relatively evolved with respect to more embedded objects. Their envelope structures and the physical conditions they reflect also may have evolved substantially from the initial core conditions. To explore this possibility, similar far-infrared observations of the envelopes of highly embedded intermediate-luminosity (i.e., 100–1000 $L_\odot$) sources are necessary. As for Herbig Ae/Be stars, models using such data as constraints can probe their envelopes. Also, comparison of the two samples can provide clues as to how physical conditions may evolve as star formation proceeds. Already, far-infrared maps (and the SED) of one such object, *IRAS* 05380−0728, have been reproduced by a spherical dust envelope model with a density distribution of $n(r) \propto r^{-0.75}$ by Colomé, Di Francesco, & Harvey (1996). This density distribution is also shallower than predicted by the standard model, but is not as shallow as required by Natta et al. (1992) for the envelopes of several Herbig Ae/Be objects.

Further observations and models of other sources are necessary to determine if general trends exist in density distribution (i.e., physical conditions) with mass and/or evolution. In this paper, the sample of high-resolution, far-infrared maps of regions containing Herbig Ae/Be stars provided by Di Francesco et al. (1994) is expanded with the inclusion of new two-dimensional (2D) and/or 1D maps of the six regions studied earlier, as well as three new regions. In addition, 10 regions containing highly embedded sources of intermediate luminosity have been observed in a similar manner. Our sample and observations are discussed in § 2. Results on locations and intensities of peak emission, as well as the sizes and shapes of sources, are shown in § 3. Inferences drawn from these data are discussed in § 4. A summary and our conclusions are found in § 5.

2. OBSERVATIONS

2.1. *Source Selection*

The Herbig Ae/Be stars in this study were chosen because they were observed by *IRAS* to have bright pointlike emission [S_ν(100 μm) > 100 Jy] associated with them. In total, nine regions containing 10 Herbig Ae/Be stars were observed (BD +40°4124 and V1686 Cyg are located in the same region). The 10 stars are listed in Table 1, along with distances, compiled by Thé et al. (1994) or Hillenbrand et al. (1992) from the literature. (The optical or "expected" posi-

TABLE 1

LIST OF OBSERVED SOURCES

Source Name	Dist.[a] (pc)	*IRAS*[b] Name	S_{IRAS}(100)[c] (Jy)	L_{IRAS}[d] ($L_\odot$)	Date[e]	G.S.D.[f] (arcsec)	Calibration[g] Object
Elias 3−1	140	04155+2812	144	9.39	1995 Aug	497	IRC +10420
AB Aur	160	04525+3028	138	9.89	1991 Dec	0	IRC +10216
MWC 137	1300	06158+1517?	337	653.	1991 Dec	294	IRC +10216
LkHα 215	800	06299+1011?	315	136.	1991 Dec	114	IRC +10216
MWC 297	450	18250−0351	1800	485.	1991 Apr[h]	0	Ceres[h]
BD +40 4124	1000	20187+4111?	880[h]	1210[i]	1991 Dec	422	IRC +10216
V1686 Cyg	1000	20187+4111?	880[h]	1210[i]	1991 Dec	441	IRC +10216
HD 200775	600	21009+6758?	1090	418.	1992 Sep	0	IRC +10420
LkHα 234	1000	21418+6552?	1210	1210	1991 Dec[h]	100	IRC +10216[h]
MWC 1080	2500	23152+6034	227	2000	1991 Dec	359	IRC +10216
IRAS 05338−0624	450	(same)	488	68.7	1991 Dec	349	IRC +10216
IRAS 05373+2349	1000	(same)	194	274.	1993 Dec	272	Ceres
IRAS 05380−0728	450	(same)	227	118.	1994 Jan	729	Ceres
IRAS 06249−1007	500	(same)	154	107.	1993 Dec	191	Ceres
IRAS 20050+2720	700	(same)	397	158.	1992 Sep	348	IRC +10420
IRAS 20081+2720	700	(same)	1317	620.	1992 Sep	635	IRC +10420
IRAS 21391+5802	750	(same)	425	139.	1992 Sep	205	IRC +10420
IRAS 21526+5728	750	(same)	207	116.	1994 Jan	422	Ceres
IRAS 22198+6336	900	(same)	415	<265.	1992 Sep	171	IRC +10420
IRAS 23568+6706	840	(same)	824	251.	1993 Dec	296	Ceres

[a] References for distance estimates are Hillenbrand et al. 1992, Elias 1978, and W89.

[b] *IRAS* sources separated from nearby Herbig Ae/Be stars by angular distances greater than their *IRAS* positional uncertainties are marked with a " ?," which indicates their questionable association.

[c] S_ν(100 μm) is *IRAS* color-corrected flux density.

[d] Integration over four *IRAS* bands; upper limits to L_{IRAS} result from upper limits at 12 μm.

[e] Date object was observed.

[f] Angular distance to guide star used during observations.

[g] Calibration object observed during the same flight series as source.

[h] Further observations made in 1992 September with IRC +10420 as calibration object.

[i] Calculated from the single *IRAS* point source in BD +40°4124 region.

TABLE 2

ASSUMED FLUX DENSITIES, OBSERVED SIZES AND OFFSETS OF CALIBRATION OBJECTS

Source Name	λ (μm)	Scan Type	S_ν (Jy)	FWHM (arcsec)	Offset (arcsec)
IRC +10216......	100	2D	790 ± 120	$(45 \pm 2) \times (32 \pm 5)$	11.
	100	1D	790 ± 120	(32 ± 2)	5.5
	50	2D	6200 ± 1300	$(35 \pm 4) \times (21 \pm 3)$	11.
	50	1D	6200 ± 1300	(28 ± 4)	7.0
IRC +10420......	100	2D	170 ± 26	$(40 \pm 2) \times (35 \pm 2)$	2.2
	100	1D	170 ± 26	(31 ± 2)	2.8
	50	2D	900 ± 190	$(29 \pm 3) \times (18 \pm 2)$	1.5
	50	1D	900 ± 190	(22 ± 2)	1.2
Ceres	100	2D	190 ± 28[a]	$(43 \pm 5) \times (37 \pm 6)$	11.
	100	1D	190 ± 28[a]	(29 ± 1)	2.2
	50	2D	520 ± 79[b]	$(35 \pm 3) \times (23 \pm 3)$	6.1
	50	1D	520 ± 79[b]	(19 ± 2)	0.62

[a] 100 μm flux density of Ceres during first two flights; reduced to 170 ± 25 on last flight.
[b] 50 μm flux density of Ceres during first two flights; reduced to 460 ± 69 on last flight.

tions of these objects can be found in Table 4.) The spectral types of our sources range from O9 (MWC 297) to A6 (Elias 3-1) with eight sources earlier than B9, which suggests a slight bias toward more massive members of the Herbig Ae/Be class. To compare with the embedded source sample (which was selected against sources with $d > 1.0$ kpc; see below), we consider only Herbig Ae/Be stars with $d \leq 1.0$ kpc. The mean distance of this subsample is 644 ± 365 pc, and the mean *IRAS* luminosity (derived using all four *IRAS* bands) is $L_{IRAS} = 497 \pm 521\ L_\odot$. Table 1 lists the name of the *IRAS* point source nearest each Herbig Ae/Be star, its color-corrected 100 μm flux density (derived following Beichmann (1985)), and its *IRAS* luminosity. Of the 10 stars observed, nine had dereddened SEDs at $\lambda < 20\ \mu$m that were modeled with optically thick disks by Hillenbrand et al. (1992). However, Elias 3-1 was the only source in a survey of nine Herbig Ae/Be stars (Di Francesco et al. 1997) to have definite interferometric evidence at millimeter wavelengths for disk-sized circumstellar structure.[2]

The embedded sources in our sample were identified by Wilking et al. (1989, hereafter W89) as potential protostellar candidates from the *IRAS* Point Source Catalog. Each source in their sample was required to be located within a known region of obscuration, have $S_\nu(60\ \mu\text{m}) > 100$ Jy, have $S_\nu(100\ \mu\text{m}) > S_\nu(60\ \mu\text{m})$, and have an *IRAS* detection at 25 μm. Taken as indicative of a color temperature, these flux densities correspond to $T < 50$ K; hence the term "cold *IRAS* source" used by W89. In addition, each source was required to have a minimum 98% correlation with the *IRAS* point source template and to have no known associations with optically identified objects. Also, the sources were restricted to be north of $\delta(1950) = -30°$, but near the galactic plane, i.e., $|b| = 2°$–$25°$. All 50 sources identified by W89 are associated with strong CO $J = 2 \rightarrow 1$ emission, and 24 exhibit high-velocity wings, which suggests extreme youth. We chose 10 sources from W89 that are at most 1.0 kpc distant but had $S_\nu(100\ \mu\text{m}) < 1500$ Jy, criteria imposed to exclude sources of high luminosity. Table 1 lists their names, distances, color-corrected 100 μm flux densities, and estimated *IRAS* luminosities. (Table 4 lists their "expected" positions from the *IRAS* Point Source Catalog.) W89 estimated the total bolometric luminosities of these sources to be 100–550 $L_\odot$, or a mass range of $\sim$3–5 $M_\odot$, assuming a main sequence mass = luminosity relationship of $(L/L_\odot) = (M/M_\odot)^4$. The mean distance of our sample is 704 ± 188 pc, and the mean *IRAS* luminosity is $212 \pm 161\ L_\odot$, reasonably similar to the mean values for the distance-restricted sample of Herbig Ae/Be stars. For 22198+6336, the upper limit to its 12 μm flux density was used to calculate the upper limit to its *IRAS* luminosity, and this limit was included in the mean.

Table 1 also lists the calibration object used for each region (IRC +10216, IRC +10420, or Ceres). Each calibration object has been shown to be pointlike at equivalent angular resolutions at far-infrared wavelengths (see Harvey et al. 1991).

2.2. *Observations and Data Reduction*

The program objects were observed from the KAO during various periods from 1991 to 1995; dates of observations are listed in Table 1. We used the University of Texas 20 channel far-infrared imaging array, a ^{3}He-cooled instrument of two columns of 10 Si bolometers aligned roughly with the elevation axis of the 0.9 m KAO telescope. This detector arrangement allowed for either 2D or 1D far-infrared mapping. Two distinct observational modes were used to create 2D or 1D maps; a "sweep" mode for stronger sources [$S_\nu(100\ \mu\text{m}) > 200$ Jy] and a "stare" mode for weaker sources [$S_\nu(100\ \mu\text{m}) < 200$ Jy]. Sweep-mode maps were created by averaging single sweeps of the array made in azimuth (for 2D maps) or elevation (for 1D maps), where each sweep was binned into 2″ or 4″ bins, along 200″ or 400″ baselines. Approximately 10 sweeps were averaged to construct either 2D or 1D maps, but 1D maps had lower noise levels because the output of 10 detectors arranged in elevation could be averaged. Stare-mode maps were created by placing the array at several positions (for 2D maps) or one position (for 1D maps) for integrations 5 or 10 s in duration, alternating with integrations of equal duration at suitable adjacent off positions. Approximately 50 integrations per sky position were averaged in this mode to produce 2D or 1D maps. Two filters, a "narrow" one centered near 100 μm and one centered near 50 μm, were used (see Harvey 1979). All nine regions containing Herbig Ae/Be stars were observed at 100 μm, and eight sources were

[2] Recently, Mannings & Sargent (1997) detected interferometrically millimeter continuum emission from seven Herbig Ae stars, of which only AB Aur appears in our sample.

observed also at 50 μm. Among the regions containing embedded sources, 10 were observed at 100 μm and seven were observed also at 50 μm.

A few Herbig Ae/Be stars in our sample were bright enough to be guided upon by the on-board tracking system of KAO. However, most Herbig Ae/Be stars and all embedded *IRAS* objects required nearby bright stars, separated by up to 750″ from the targets, for guiding. In these cases, the array was offset from the optical position of the guide star to the position of the target prior to observations. Table 1 also lists the angular displacement of the guide stars, or guide star distances (GSDs), from each program object.

In every map, spikes greater than 5 σ were replaced by the average of data in adjacent bins. Spatial frequencies in the data exceeding that possible given the resolution of the telescope were filtered out. In general, sweep-mode observations were processed more than stare-mode observations. For example, background emission levels were removed from sweep data by subtracting the averages of several bins on the ends of each sweep. Also, each sweep was cross-correlated with a Gaussian to determine corrections from possible positional drifts. Further shifts were applied to correct for the separation between columns in 2D sweep maps. Data from either mode were then averaged in spatial pixels of size approximately that of the 2″ or 4″ spatial bins of each baseline.

Two-dimensional maps were analyzed using routines in the Astronomical Image Processing System (AIPS) , and all sources in 2D maps were fitted with elliptical Gaussians to determine their sizes. One-dimensional maps were analyzed similarly, except a 1D Gaussian fitting algorithm was used to determine source sizes (see, e.g., Bevington 1969, p. 204). Conversion factors from observed counts to intensities were determined from unresolved calibration objects and applied to the program objects. Flux densities were obtained by integrating maps either within a box surrounding the source (for 2D maps) or along the baseline (for 1D maps).

2.3. *Flux Calibration*

Although the KAO had an on-board radiometer for the monitoring of water vapor levels at the zenith, it did not perform consistently enough during our flights to allow us to correct for residual atmospheric absorption. An additional 30% uncertainty was included in all flux density estimates at both wavelengths to account for the possibility of different attenuation toward the program sources and calibration objects.

Far-infrared flux densities of Ceres (for 1993 December/1994 January) were estimated using the HOTROCK program of G. Doppmann (1996, private communication), which assumes that Ceres is a slowly rotating sphere of constant albedo. A diameter of 845 km was assumed, equal to the average diameter determined for Ceres in the *IRAS* Minor Planet Survey from all four *IRAS* bands (Tedesco et al. 1992). The intrinsic accuracy of the HOTROCK program to predict the actual *IRAS* flux densities of Ceres in the far-infrared is $\sim 15\%$, a factor included in estimates of uncertainty. Flux densities of Ceres were determined to be $S_\nu(100\ \mu\text{m}) = 188$ Jy and $S_\nu(50\ \mu\text{m}) = 524$ Jy during the 1993 December flights, which decreased to $S_\nu(100\ \mu\text{m}) = 165$ Jy and $S_\nu(50\ \mu\text{m}) = 462$ Jy during the 1994 January flight.

For IRC +10216 and IRC +10420, far-infrared flux densities were obtained from the *IRAS* Point Source Catalog at all four bands and color-corrected assuming intrinsic power-law SEDs (see Beichmann 1985). (IRC +10216 and IRC +10420 both may vary significantly in the far-infrared, but the extent of their possible variability is not well documented.) This procedure yielded $S_\nu(60\ \mu\text{m}) = 4010$ Jy and $S_\nu(100\ \mu\text{m}) = 795$ Jy for IRC +10216, and $S_\nu(60\ \mu\text{m}) = 579$ Jy and $S_\nu(100\ \mu\text{m}) = 170$ Jy for IRC +10420. Maximum uncertainties of flux densities after color correction were estimated to be $\sim 15\%$. These corrected flux densities (and those at 12 and 25 μm) were then used to estimate the 50 μm flux densities, using an interpolation algorithm that forces matching of values and slopes at each *IRAS* wavelength (see, e.g., Press et al. 1986). This procedure yielded $S_\nu(50\ \mu\text{m}) = 6210$ Jy for IRC +10216, and $S_\nu(50\ \mu\text{m}) = 900$ Jy for IRC +10420 (each with estimated uncertainties of $\sim 21\%$).

3. RESULTS

3.1. *Calibration*

Far-infrared 2D and 1D maps of calibration object IRC +10216 are presented in Figure 1 as an example of a bright, unresolved object. For all calibration objects, the assumed flux densities (S_ν), average measured sizes (FWHMs) of the major and minor axes of the beam ellipses, and average measured offsets of actual peak intensity positions from expected (i.e., optical) positions are listed in Table 2. Each calibration object is pointlike at our resolution; hence they measure beam shapes and sizes. These shapes are elliptical due to the rectangular shape of the detectors and diffraction, with major to minor axis (aspect) ratios of 1.24 at 100 μm and 1.60 at 50 μm, on average. The average geometrical means of the 2D beam FWHMs are 38″ at 100 μm and 26″ at 50 μm. Beams from 2D observations were slightly larger than beams from 1D observations, a difference probably due to small differences in 2D and 1D data reduction. The observed sizes of calibration objects were roughly consistent between flights and flight series. The angular distances between the observed and predicted peaks of emission of calibration objects are all less than half one beamwidth at both wavelengths. The larger offsets (see Table 2) for IRC +10216 illustrate the increased positional uncertainties that result from guiding on a nearby star, rather than guiding on the object itself. Although size data were consistent between calibration objects, source data were compared only to those of calibration objects observed during the same flight series.

3.2. *Maps of Program Regions*

Maps of all sources detected at either 100 or 50 μm are presented in Figures 2–10 (Herbig Ae/Be stars), and Figures 11–20 (embedded *IRAS* sources), superposed onto optical images taken from the Digital Sky Survey[3] using B1950.0 coordinates. For 1D maps, coordinates are relative to the position of peak emission, which is shown in an adjacent 2D image.

[3] Based on photographic data obtained using the Oschin Schmidt Telescope on Palomar Mountain. The Palomar Sky Survey was funded by the National Geographic Society. The Oschin Schmidt Telescope is operated by the California Institute of Technology and Palomar Observatory. The plates were processed into the present compressed digital format with their permission. The Digitized Sky Survey was produced at the Space Telescope Science Institute (STScI) under U.S. Government grant NAG W-2166.

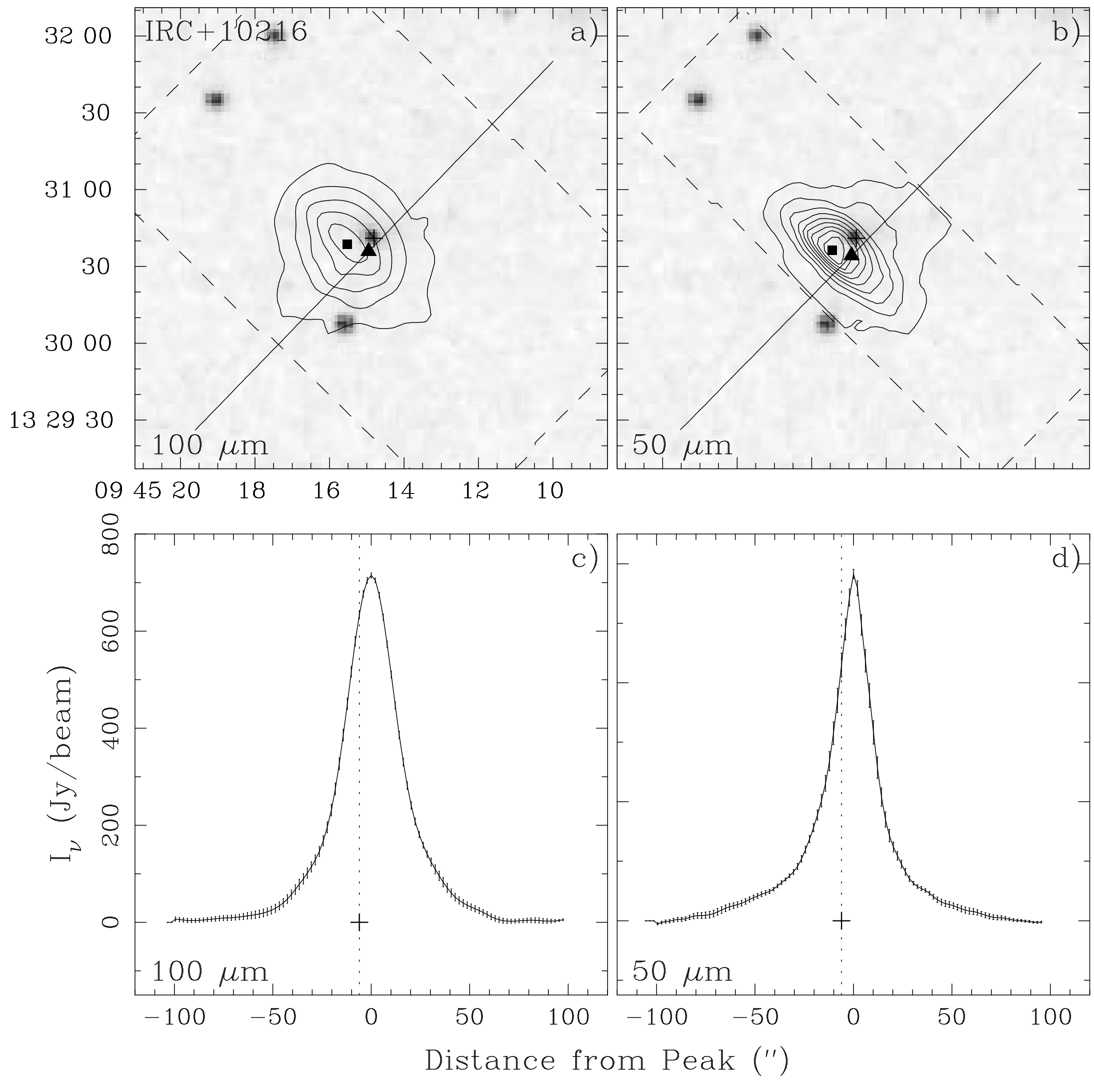

FIG. 1.—Far-infrared 2D and 1D maps of calibration object IRC +10216. For 2D maps, positions are given in B1950.0 coordinates. Solid contours represent levels of constant intensity, crosses are the positions of program sources, and squares are the peak of far-infrared emission. Dashed lines surrounding the contours of 2D maps indicate their extent. Solid lines across this extent show the locations of 1D observations (in panel below). Triangles denote the positions of peak intensity in 1D maps. For 1D maps, error bars represent rms levels at each pixel; because of spatial oversampling, the uncertainties from bin-to-bin are correlated and therefore only represent variations on the scale of the beam. The vertical dotted lines (with *crosses*) in 1D map panels denote the positions of the program objects projected onto the 1D map. Dashed lines show the 1D profiles of appropriate calibration objects (see Table 1), normalized to the peak intensity of the program source, for comparison. (*a*) 100 μm 2D map with contours starting at and increasing in steps of 10 σ (123.9 Jy beam^{-1}) overlaid onto a Digital Sky Survey image of region. (*b*) 50 μm 2D map with contours starting at and increasing in steps of 10 σ (538.0 Jy beam^{-1}) overlaid onto a Digital Sky Survey image of region. (*c*) 100 μm 1D profile with 1 σ error bars. (*d*) 50 μm 1D profile with 1 σ error bars.

All 19 program regions were observed at 100 μm, and 15 of these regions were also observed at 50 μm. At 100 μm, 2D maps were made of 18 regions and 1D maps were made of 13. At 50 μm, 2D maps were made of 12 regions and 1D maps were made of seven. A source was considered detected only if the peak intensity in the region (I_ν) exceeded 5 σ. In cases where a source was not detected, an upper limit to the flux density was determined by adding the flux density measured in the field around the expected position of the source to the uncertainty. Two sources, *IRAS* 21526+5728 (Fig. 18) and *IRAS* 23568+6706 (Fig. 20), were not detected in 2D maps at 100 μm but were detected in 1D maps with lower noise. Two sources, *IRAS* 05338−0624 and *IRAS* 23568+6706, were not detected in 2D maps at 50 μm; only the former source was observed and detected in a 1D map with lower noise (Fig. 11). The 100 μm 2D map and the 50 μm 1D map of the Elias 3-1 region (Fig. 2), as well as the 50 μm 2D maps of the MWC 137 region (Fig. 4) and the HD 200775 region (Fig. 8) do not include the entire far-infrared source. Flux densities derived from these maps are lower limits. In addition, accurate size information could not be obtained from the latter two 50 μm 2D maps.

One far-infrared source is found per region in most maps with detections, although secondary peaks may be seen in the 100 μm 1D maps of LkHα 215 (Fig. 5) and *IRAS* 23568+6706 (Fig. 20). The peak intensities (I_ν), total flux densities (S_ν), sizes (FWHM), and position angles (PA) of these sources are listed in Table 3. The 1 σ noise levels in I_ν were calculated from the mean of uncertainties in all bins and the rms variation of the baseline or background, added in quadrature. Uncertainties of S_ν include contributions from the 1 σ noise levels, uncertainties in the flux densities and sizes of the calibration objects, and possible residual differences in water vapor absorption between the sources

TABLE 3

OBSERVED PEAK INTENSITIES, FLUX DENSITIES, AND SIZES OF PROGRAM OBJECTS

Source Name	λ (μm)	Scan Type	S_ν (Jy)	I_ν (Jy beam^{-1})	Size (arcsec)	P.A. (deg)
Elias 3-1	100	2D	150 ± 87	36.8 ± 4.70	(111 ± 11) × (49 ± 20)	61 ± 7
	50	1D	86 ± 45	59.1 ± 5.45	(25 ± 4)	129 ± 3
AB Aur	100	2D	85 ± 48	70.6 ± 7.35	(46 ± 8) × (34 ± 4)	328 ± 6
	100	1D	75 ± 35	69.2 ± 1.98	(31 ± 2)	308 ± 3
	50	2D	110 ± 67	105 ± 8.56	(32 ± 3) × (20 ± 4)	39 ± 5
MWC 137	100	2D	330 ± 160	116 ± 8.70	(82 ± 6) × (63 ± 11)	58 ± 10
	100	1D	220 ± 99	93.8 ± 3.80	(70 ± 2)	348 ± 3
	50	2D	130 ± 80	75.2 ± 14.0	...	...
	50	1D	270 ± 140	101 ± 11.5	(81 ± 3)	349 ± 3
LkHα 215	100	2D	240 ± 130	61.5 ± 10.4	(94 ± 32) × (64 ± 24)	79 ± 10
	100	1D	180 ± 94	53.4 ± 6.74	(78 ± 9)	354 ± 5
MWC 297	100	2D	1300 ± 640	298 ± 8.98	(61 ± 11) × (54 ± 14)	309 ± 10
	100	1D	640 ± 290	257 ± 8.25	(66 ± 6)	216 ± 5
	50	2D	1100 ± 540	273 ± 23.1	(57 ± 13) × (46 ± 15)	292 ± 10
	50	1D	660 ± 310	245 ± 14.7	(57 ± 4)	204 ± 3
BD +40 4124......	100	2D	730 ± 380	262 ± 13.2	(59 ± 7) × (41 ± 10)	154 ± 5
region	50	2D	680 ± 390	262 ± 30.7	(58 ± 19) × (43 ± 14)	116 ± 10
HD 200775.........	100	2D	890 ± 440	212 ± 13.8	(85 ± 7) × (64 ± 6)	241 ± 5
	50	2D	980 ± 520	212 ± 34.6	...	...
LkHα 234	100	2D	1200 ± 630	432 ± 16.1	(62 ± 8) × (46 ± 12)	158 ± 10
	100	1D	850 ± 420	499 ± 7.91	(52 ± 6)	82 ± 3
	50	2D	980 ± 550	405 ± 36.7	(45 ± 9) × (35 ± 10)	153 ± 5
	50	1D	830 ± 430	512 ± 21.2	(46 ± 7)	79 ± 3
MWC 1080.........	100	2D	200 ± 100	112 ± 11.4	(50 ± 3) × (44 ± 7)	196 ± 5
	100	1D	180 ± 85	129 ± 4.43	(43 ± 2)	98 ± 3
	50	2D	200 ± 110	113 ± 9.44	(44 ± 8) × (34 ± 7)	176 ± 10
05338-0624	100	2D	430 ± 220	241 ± 11.9	(51 ± 8) × (39 ± 6)	68 ± 5
	100	1D	280 ± 130	239 ± 5.03	(34 ± 2)	356 ± 3
	50	2D	<350	146 ± 30.4	...	...
	50	1D	320 ± 170	213 ± 20.8	(32 ± 3)	359 ± 3
05373+2349	100	2D	270 ± 180	170 ± 16.2	(62 ± 2) × (40 ± 3)	55 ± 5
05380−0728	100	2D	210 ± 150	110 ± 9.12	(49 ± 5) × (44 ± 9)	115 ± 5
06249−1007	100	1D	240 ± 120	136 ± 6.68	(45 ± 3)	4 ± 3
20050+2720	100	2D	550 ± 300	300 ± 19.2	(51 ± 3) × (46 ± 3)	113 ± 9
	100	1D	400 ± 190	289 ± 5.83	(39 ± 2)	60 ± 3
	50	1D	240 ± 130	125 ± 9.80	(35 ± 4)	59 ± 3
20081+2720	100	2D	1900 ± 930	302 ± 14.6	(91 ± 6) × (70 ± 9)	160 ± 5
	50	2D	1100 ± 600	245 ± 36.8	(71 ± 8) × (52 ± 11)	170 ± 5
21391+5802	100	2D	430 ± 230	195 ± 15.1	(52 ± 4) × (49 ± 5)	296 ± 4
	100	1D	280 ± 140	188 ± 7.76	(39 ± 1)	238 ± 3
	50	2D	320 ± 150	108 ± 15.8	(51 ± 4) × (40 ± 9)	307 ± 4
21526+5728	100	2D	<220	72.4 ± 15.5	...	...
	100	1D	160 ± 73	64.3 ± 3.53	(61 ± 5)	83 ± 5
	50	1D	53 ± 25	46.2 ± 3.43	(28 ± 3)	75 ± 3
22198+6336	100	2D	310 ± 130	168 ± 14.5	(52 ± 3) × (45 ± 4)	248 ± 5
	100	1D	230 ± 120	166 ± 5.45	(37 ± 2)	160 ± 4
	50	2D	270 ± 110	125 ± 13.9	(35 ± 3) × (29 ± 5)	67 ± 5
23568+6706	100	2D	<640	160 ± 22.4	...	...
	100	1D	180 ± 91	96.7 ± 8.25	(86 ± 13)	134 ± 3
	50	2D	<220	104 ± 32.6	...	...

and the calibrators (see § 2.3). For 2D maps, the position angles are the angle of major axis of the 2D Gaussian fit counterclockwise with respect to north. For 1D maps, the position angles are the angle of the direction of the map, from positive to negative offsets, counterclockwise with respect to north.

3.3. *Positions and Source Identifications*

The embedded objects in our sample were identified directly by *IRAS*; however, it is not clear how the Herbig Ae/Be stars in our sample are associated with the far-infrared emission in their respective regions. As described earlier (§ 2.1), many Herbig Ae/Be stars in our sample are located outside the error ellipses of the nearest *IRAS* point source (see Table 1). On the other hand, the corresponding *IRAS* flux densities of these sources have been included in the SEDs of the Herbig Ae/Be stars, albeit with reservations (see Hillenbrand et al. 1992). Our high-resolution maps of the regions in our sample allow us to test the association of some Herbig Ae/Be stars with *IRAS* sources. Table 4 lists the expected and observed peak positions in B1950.0 coordinates from the observations of all 19 program regions and the angular offsets between these positions. (By "expected" we mean the position of the visible star for the Herbig Ae/Be stars and the *IRAS* position for the embedded sources.)

First, potential uncertainties in position arising from guiding on a nearby, bright star, rather than the Herbig Ae/Be star itself, must be addressed. Positional discrepancies can arise owing to errors in the guide star position,

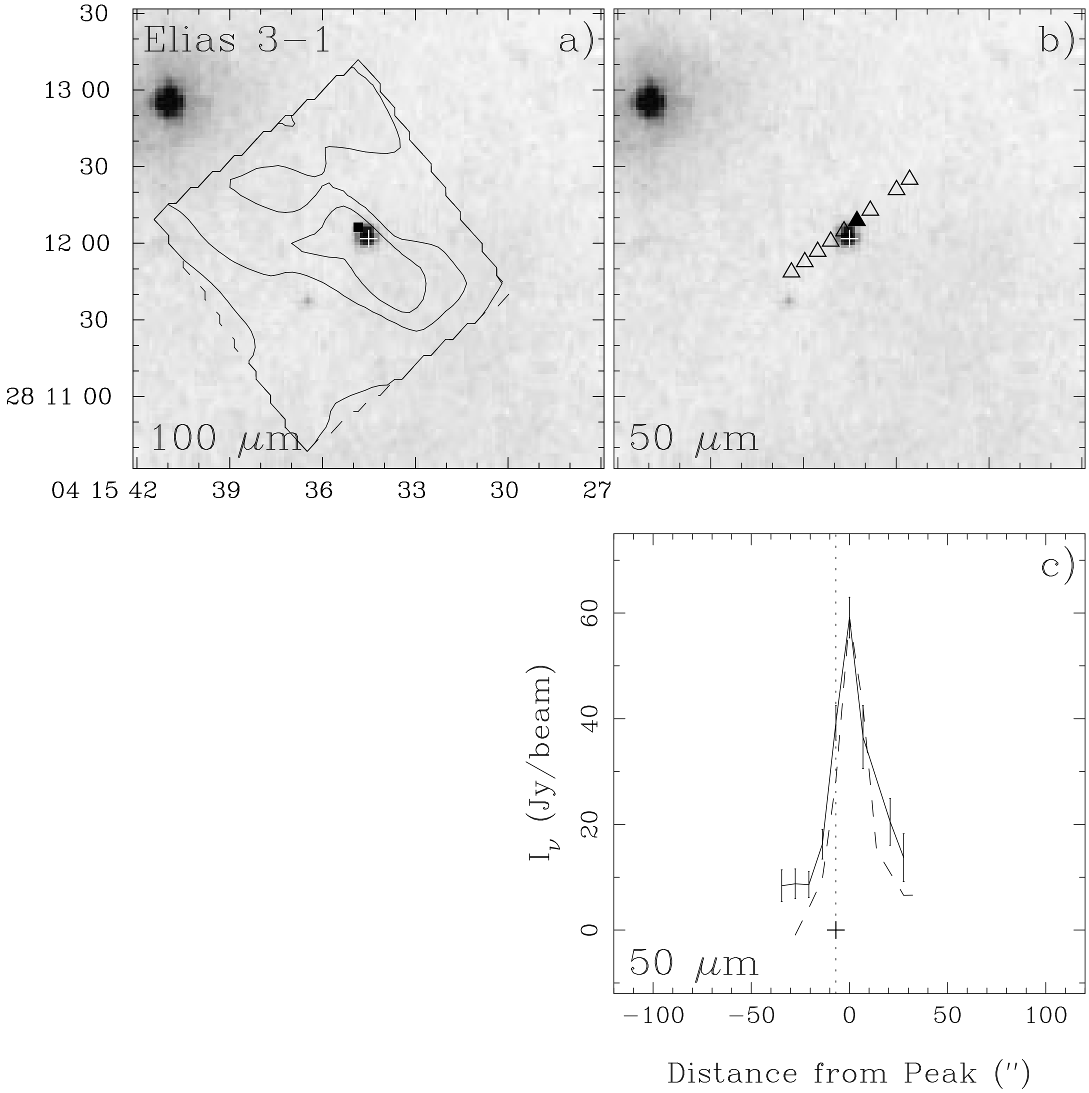

FIG. 2.—Far-infrared 2D and 1D maps of region containing Elias 3-1. See Fig. 1 for symbol/line definitions, but note that open triangles here denote the positions of individual detectors in 1D stare-mode maps. (*a*) 100 μm 2D map with contours starting at and increasing in steps of 2 σ (9.4 Jy beam^{-1}) overlaid onto Digital Sky Survey image of region. (*b*) Locations of 50 μm 1D map overlaid onto Digital Sky Survey image of region. (*c*) 50 μm 1D profile with 1 σ error bars.

rotation of field, or plate scale (see § 2.2). We use the embedded objects to determine the accuracy of our pointing with increasing GSD (i.e., the angular separation between program object and guide star positions) by measuring differences between their positions of peak intensity (I_ν) in our 2D maps and their positions listed in the *IRAS* Point Source Catalog. We can apply this information to decide whether or not the far-infrared emission peaks on the Herbig Ae/Be stars. Both subsamples were observed with a similar range of GSDs, i.e., between 0″ and 750″.

Examining only 2D maps to ensure that the peaks of emission were observed, we find that the peaks of all 10 embedded sources are within half of the KAO beam of the *IRAS* position. This result suggests that any objects more than a half-beam away from our peak position are unlikely to be associated. However, only five of 10 embedded objects peaked within the *IRAS* error ellipses. The remaining five objects are likely still related to the *IRAS* point sources, since they were observed with guide stars most distant from the targets in our sample (i.e., greater than 340″). Figure 21 shows the general increase of positional offset with GSD for the embedded sample (and calibrators) for 2D maps at both 100 and 50 μm. Least-squares fits to these samples (also shown in Fig. 21) have correlation coefficients of $r = 0.88$ and $r = 0.70$ for 100 and 50 μm maps, respectively. Given that the association of these far-infrared objects with the *IRAS* sources is fairly unambiguous, these fits provide an empirical means to gauge how positional uncertainties increase with GSD for all of our data.

In general, only some maps of regions containing Herbig Ae/Be stars show well-associated far-infrared emission. For example, only six of 10 Herbig Ae/Be stars surveyed are located within a half–KAO beamwidth of observed peaks of far-infrared emission (e.g., $\sim$15″–20″ at 100 μm). Furthermore, only four of these six stars (AB Aur, Elias 3-1, MWC 297, and MWC 1080) also lie within the *IRAS* error ellipses of the nearest *IRAS* point source (see Table 1). Besides Elias 3-1, these objects were bright enough to be observed without requiring a separate guide star (i.e., zero GSD), so positions of I_ν in the KAO maps should be relatively accurate. (For MWC 297, however, a large positional offset was found at 100 μm, but was still consistent with

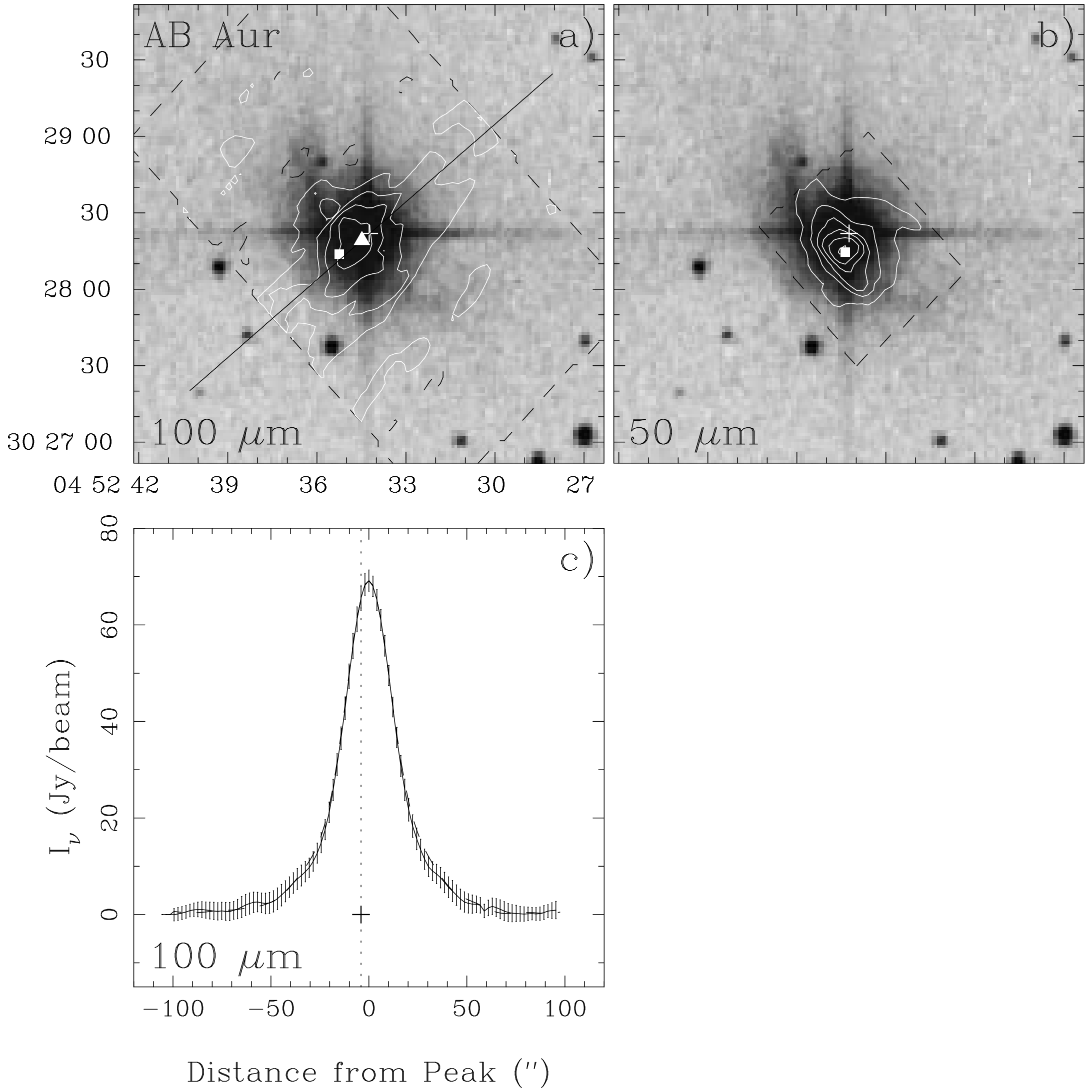

FIG. 3.—Far-infrared 2D and 1D maps of region containing AB Aur. See Fig. 1 for symbol/line definitions. (*a*) 100 μm 2D map with contours starting at and increasing in steps of 2 σ (14.7 Jy beam^{-1}) overlaid onto Digital Sky Survey image of region. (*b*) 50 μm 2D map with contours starting at and increasing in steps of 2 σ (17.1 Jy beam^{-1}). (*c*) 100 μm 1D profile with 1 σ error bars.

both the half–KAO beamwidth and the local *IRAS* ellipse. This large offset also was not seen in the 50 μm map of the region.) For Elias 3-1, a guide star $\sim$500″ distant was used, but the local position of I_ν is still relatively close by (6″.2) despite the widespread emission in the region (see Fig. 2).

Other regions containing Herbig Ae/Be stars show less well-associated far-infrared emission. For example, the other 2 stars located within half–KAO beamwidths of the peaks of far-infrared emission, LkHα 215 and LkHα 234, are located outside error ellipses of the nearest *IRAS* point sources. However, these two sources were observed with guide stars located, respectively, 110″ and 100″ distant, and their offsets are consistent with those expected from such GSDs (see Fig. 21). Therefore, the data from these regions are consistent with the far-infrared emission surrounding the stars themselves (see Figs. 4 and 9). No such explanation exists for the large offsets seen for the other four Herbig stars in our sample, MWC 137, HD 200775, and BD +40°4124 (with nearby V1686 Cyg). Each star is displaced significantly from the peaks of far-infrared emission in their respective regions, and displaced much more than can be accounted for by positional uncertainties (see Fig. 21). The significance of these displacements is discussed in § 4.1.

3.4. *Observed Flux Densities and Source Sizes*

Flux densities of all objects (or upper limits) were calculated only from 2D maps of each source because 1D maps might miss considerable emission in directions orthogonal to the cuts. Derived 100 μm flux densities [S_ν(KAO)] were then compared with color-corrected 100 μm flux densities from the *IRAS* Point Source Catalog [S_ν(*IRAS*)] to determine if a significant decrease in S_ν accompanied the decrease in beam size.

Lower far-infrared flux densities than observed by *IRAS* might be expected from KAO observations, since the potential for unrelated or diffuse sources of emission to be included within the smaller KAO beam is reduced. However, only a single far-infrared source per region was found in most of our 2D maps. After color correction (using the same method used for the calibrators, as described in § 2.3), good agreement is found between S_ν(KAO) and S_ν(*IRAS*) at 100 μm for all sources. The ratio of S_ν(KAO) to S_ν(*IRAS*) at 100 μm for all 16 detected sources in 2D maps

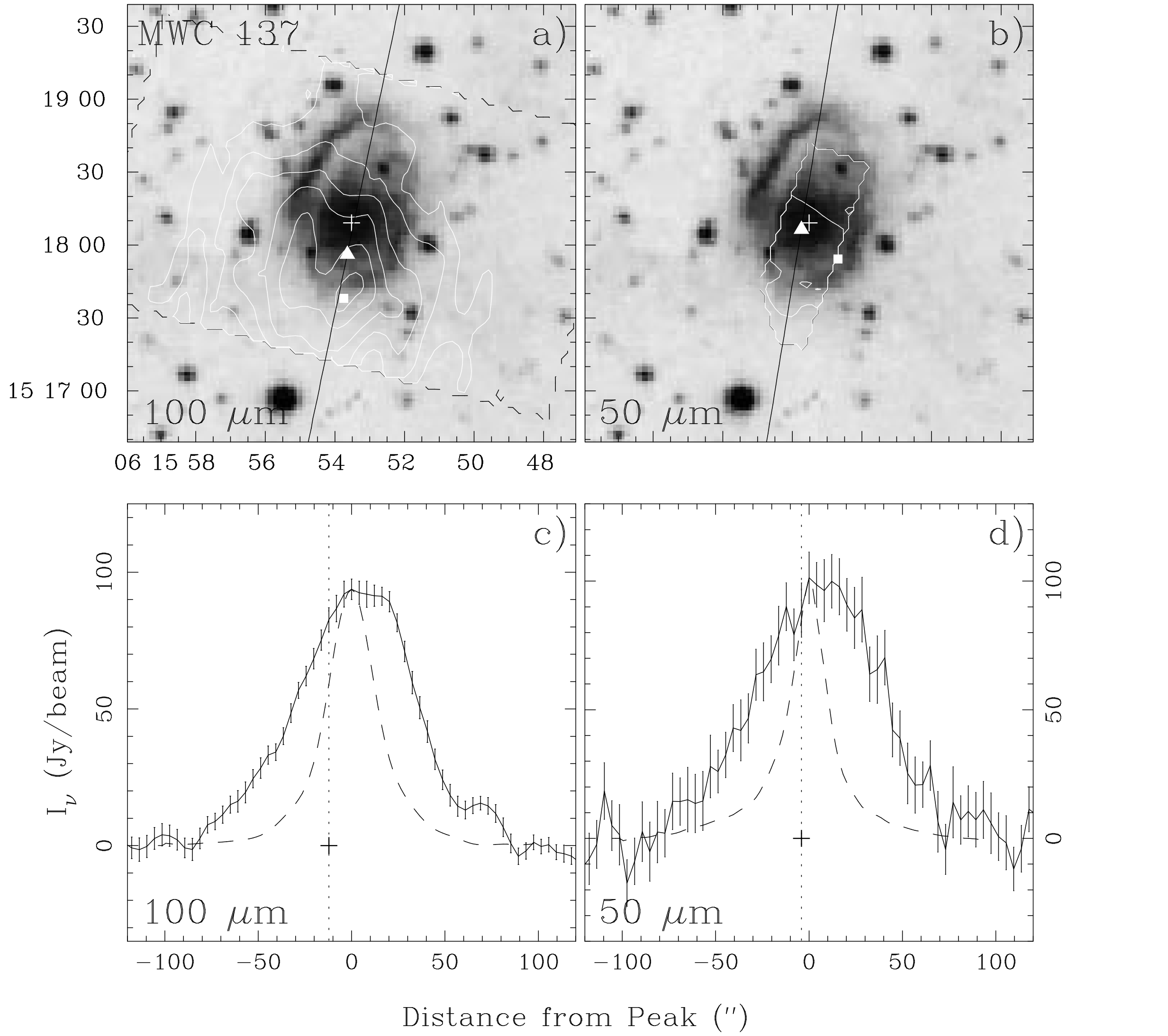

FIG. 4.—Far-infrared 2D and 1D maps of region containing MWC 137. See Fig. 1 for symbol/line definitions. (*a*) 100 μm 2D map with contours starting at and increasing in steps of 2 σ (17.4 Jy beam^{-1}) overlaid onto Digital Sky Survey image of region. (*b*) 50 μm 2D map with contours starting at and increasing in steps of 2 σ (29.9 Jy beam^{-1}) overlaid onto Digital Sky Survey image of region. (*c*) 100 μm 1D profile with 1 σ error bars. (*d*) 50 μm 1D profile with 1 σ error bars.

has a mean of 0.96 $\pm$ 0.25 (standard deviation). In addition, S_ν(KAO) is consistent within uncertainties with S_ν(*IRAS*) at 100 μm for each source individually. However, we find flux densities at 50 μm to be slightly larger than expected given the overall *IRAS* far-infrared SEDs of all eight cases where S_ν(KAO) is available. For example, the ratio of S_ν(KAO) at 50 μm to S_ν(*IRAS*) at 60 μm for all eight detected cases has a mean of 1.41 $\pm$ 0.39 (standard deviation). High values of S_ν(KAO) at 50 μm, however, appear significant for only *IRAS* 22198+6336 and *IRAS* 21391+5802. Both maps were obtained on the same flight in 1992 September, and the large offset may be due to increased water vapor absorption toward the flux calibrator relative to these objects during that one flight.

To determine if the detected sources were significantly extended (i.e., at a level greater than 1 σ) with respect to the calibration sources, FWHMs of the 2D or 1D Gaussian fits of program source maps were compared with those of relevant calibration objects. The FWHMs of Gaussian fits for almost every far-infrared source are larger than those of calibration objects at both 100 and 50 μm, which indicates that the sample is mostly extended significantly at the spatial resolutions of KAO at both wavelengths. (For 1D profiles, the differences between observed program source and observed calibration " point source " object sizes can be seen readily in the 1D profile frames of Figures 2–20.) A substantial range in extent is found in the sample. Some sources (e.g., those in the Elias 3-1 region [see Fig. 2] or the *IRAS* 20081+2720 region [see Fig. 16]) are very extended, while others (e.g, those in the BD +40°4124 region [see Fig. 7] or the *IRAS* 05380−0728 region [see Fig. 13]) are just over 1 σ larger than the beam at 100 μm. Only sources associated with AB Aur (see Fig. 3) and possibly *IRAS* 05338−0624 (see Fig. 11) are not significantly extended (at both 100 and 50 μm) in both 2D and 1D maps. Thus, only these two sources are considered potentially unresolved in our sample. The linear sizes or upper limits obtained from deconvolutions of all maps by beams are discussed in § 4.3.

4. DISCUSSION

4.1. *Offset Far-Infrared Sources in Herbig Ae/Be Regions*

The optical positions of four Herbig Ae/Be stars (MWC 137, BD +40°4124, V1686 Cyg, and HD 200775; see Figs.

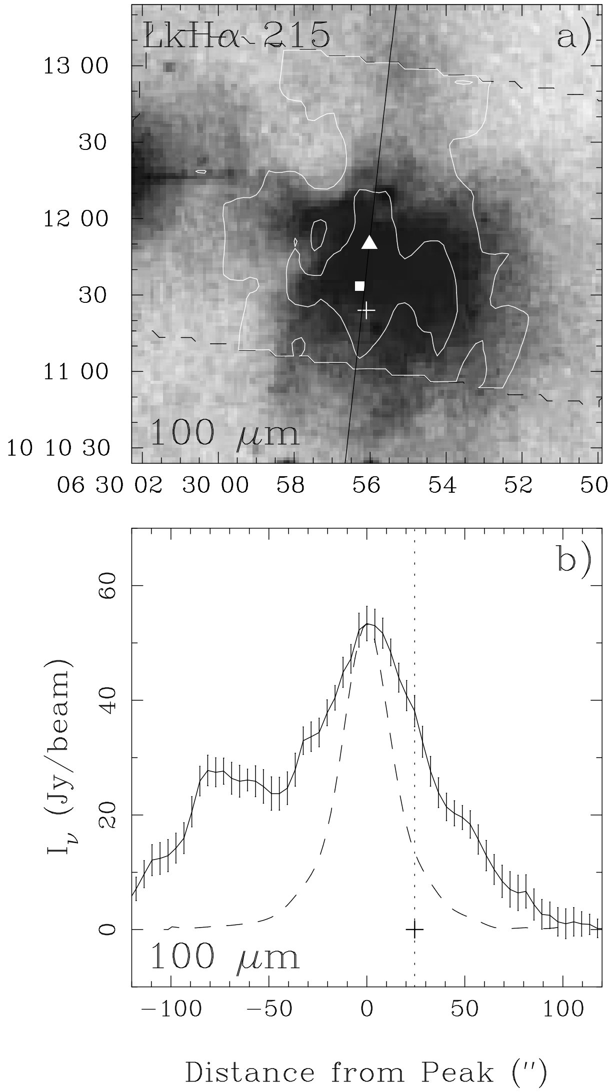

FIG. 5.—Far-infrared 2D and 1D maps of region containing LkHα 215. See Fig. 1 for symbol/line definitions. (*a*) 100 μm 2D map with contours starting at and increasing in steps of 2 σ (20.8 Jy beam^{-1}) overlaid onto Digital Sky Survey image of region. (*b*) 100 μm 1D profile with 1 σ error bars.

4, 7, and 8) are displaced from the nearest peaks of far-infrared emission by more than a half–KAO beamwidth, more than can be accounted for by increased pointing uncertainties due to distant guide stars (see Fig. 21). For these regions, these significant offsets imply the optical objects are not immediately surrounded by an envelope of far-infrared emitting dust. Instead, the emission probably comes from dust situated at a position adjacent to the optical objects; this dust may be heated either internally from highly embedded (optically invisible) objects, or externally by the Herbig stars themselves, or both. These regions are examined individually in this section.

4.1.1. *The MWC 137 Region*

Figure 4 shows MWC 137 situated in the center of an oval reflection nebula. Figure 22*a* shows the relative positions of the optical and 100 μm objects in the region. MWC 137 is located ∼10″ north of the nearest *IRAS* point source, just outside its positional error ellipse. Our 2D 100 μm map shows a wide area of bright far-infrared emission around the nebulosity, but peaking ∼30″ south of MWC 137 itself; however, the peak in the 2D 100 μm map may not be well defined, considering the flat distribution of emission near the maximum. Unfortunately, our 50 μm (stare-mode) map clearly did not cover the entire source. Our 1D 100 μm and 1D 50 μm maps show profiles with surprisingly similar widths, but also with flat maxima. The peaks of these profiles are much closer to the optical position of MWC 137 (13″ and 4″.3 south of MWC 137, at 100 and 50 μm, respectively). In fact, these flat maxima include the MWC 137 position, which suggests MWC 137 is indeed immediately surrounded by far-infrared emitting dust. Di Francesco et al. (1997) detected interferometrically only a single millimeter continuum source at a position ∼3″ south-by-southwest, between a half- and a full-beamwidth, from MWC 137. In addition, all our maps peak south of MWC 137, more consistent with the position of the southern *IRAS* point source. Therefore, a source of the far-infrared emission in the region spatially distinct from MWC 137 remains possible. Far-infrared maps of even higher spatial resolution are required to untangle this situation.

4.1.2. *The BD +40°4124 Region*

The BD +40°4124 region contains many infrared-bright sources, including both Herbig Ae/Be stars, BD +40°4124 and V1686 Cyg (Hillenbrand et al. 1995; see Fig. 7). Figures 22*b* and 22*c* show the *IRAS* point source located between these two stars and a third object to the east, V1318 Cyg. Despite the proximity of all three stars to each other, all of them lie outside the *IRAS* positional error ellipse, which makes it unclear which objects are actually associated with the far-infrared emission. Our 2D 100 μm map, however, peaks much closer to V1318 Cyg (10″ offset) than to BD +40°4124 (36″ offset) or V1686 Cyg (22″ offset). Also, the measured offset to V1318 Cyg is more consistent with the relationship shown in Figure 21 between the positional uncertainty and the GSD. If either BD +40°4124 or V1686 were the actual source of the emission, the positional offsets would be far from the usual relation. This map suggests V1318 Cyg is the one object immediately surrounded by far-infrared emitting dust in the region; however, the 50 μm data, with higher spatial resolution, is less clear since it reveals a peak near-equidistant from V1318 Cyg (17″ offset), V1686 Cyg (17″ offset), and BD +40°4124 (19″ offset). V1318 Cyg was recently identified as the peak of local 800 μm emission by Aspin, Sandell, & Weintraub (1994). In addition, only V1318 Cyg (but not BD +40°4124 or V1686 Cyg) had compact 2.7 mm emission detected interferometrically by Di Francesco et al. (1997). These results further suggest V1318 Cyg is immediately surrounded by more dust than either BD +40°4124 or V1686 Cyg. External heating by BD +40°4124 and/or V1686 Cyg, however, may still be significant given the close proximity of all three objects.

4.1.3. *The HD 200775 Region*

The region containing HD 200775 (NGC 7023; see Fig. 8) is the only one in our sample that contains an optical source (HD 200775 itself), a nearby *IRAS* source (*IRAS* 21009+6758), and far-infrared emission in our KAO maps, all of which are outside the positional uncertainties of each other (see Fig. 22*d*). The offsets measured between the star and peaks at both 100 (50″) and 50 μm (37″) are the largest in our entire sample. As with the MWC 137 region, our 50 μm map did not effectively cover the entire far-infrared source, which makes a determination of the peak position very inaccurate. HD 200775 was itself optically bright enough to be observed without requiring a separate guide

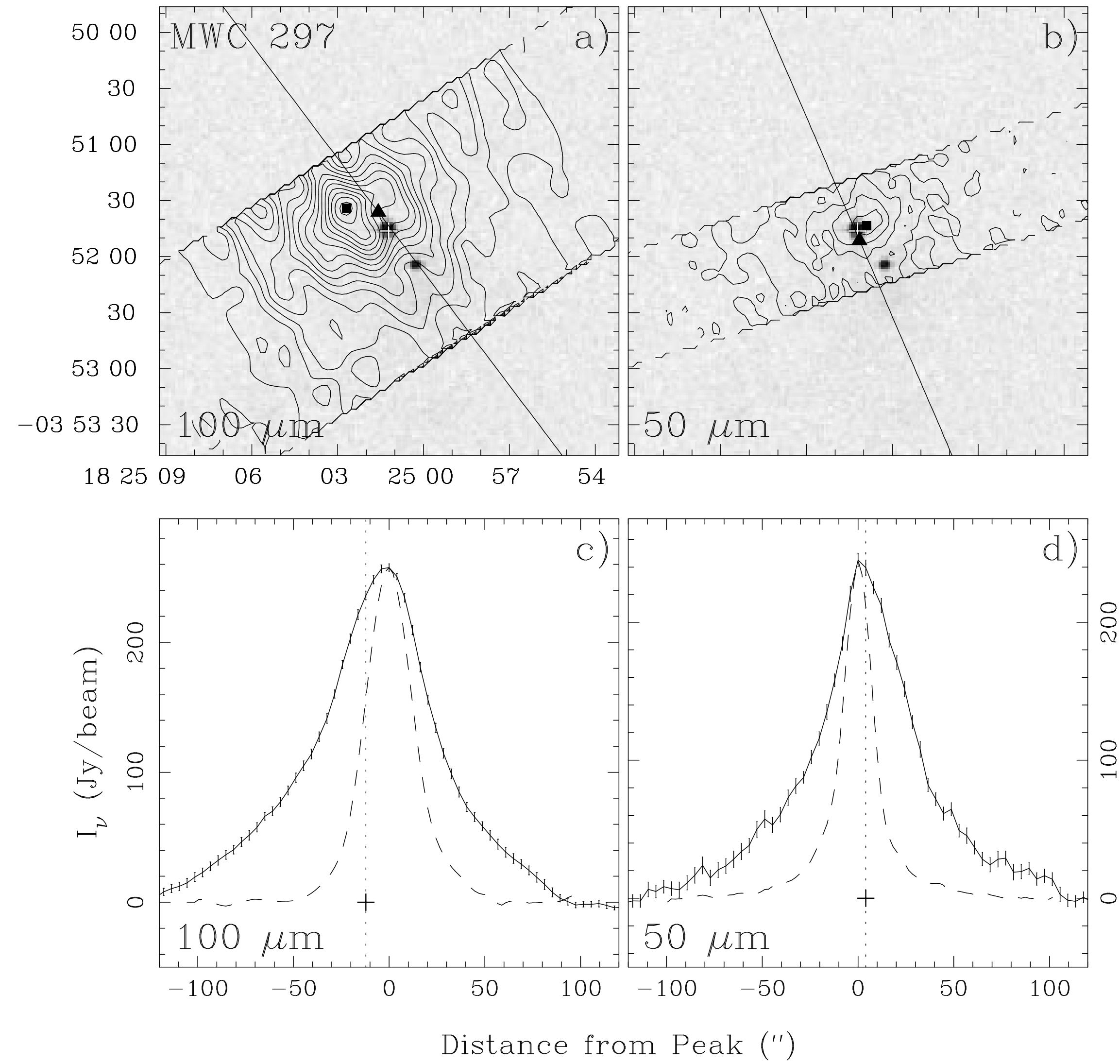

FIG. 6.—Far-infrared 2D and 1D maps of region containing MWC 297. See Fig. 1 for symbol/line definitions. (*a*) 100 μm 2D map with contours starting at and increasing in steps of 2 σ (18.0 Jy beam^{-1}) overlaid onto Digital Sky Survey image of region. (*b*) 50 μm 2D map with contours starting at and increasing in steps of 2 σ (46.2 Jy beam^{-1}) overlaid onto Digital Sky Survey image of region. (*c*) 100 μm 1D profile with 1 σ error bars. (*d*) 50 μm 1D profile with 1 σ error bars.

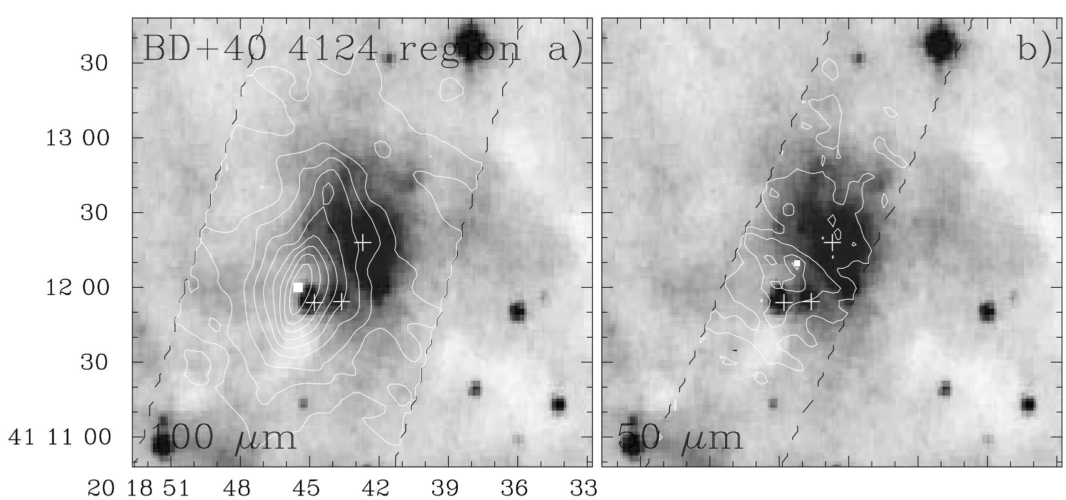

FIG. 7.—Far-infrared 2D maps of region containing BD +40°4124, V1686 Cyg, and V1318 Cyg (denoted as crosses, respectively, from west to east). See Fig. 1 for symbol/line definitions. (*a*) 100 μm 2D map with contours starting at and increasing in steps of 2 σ (26.4 Jy beam^{-1}) overlaid onto Digital Sky Survey image of region. (*b*) 50 μm 2D map with contours starting at and increasing in steps of 2 σ (61.4 Jy beam^{-1}) overlaid onto Digital Sky Survey image of region.

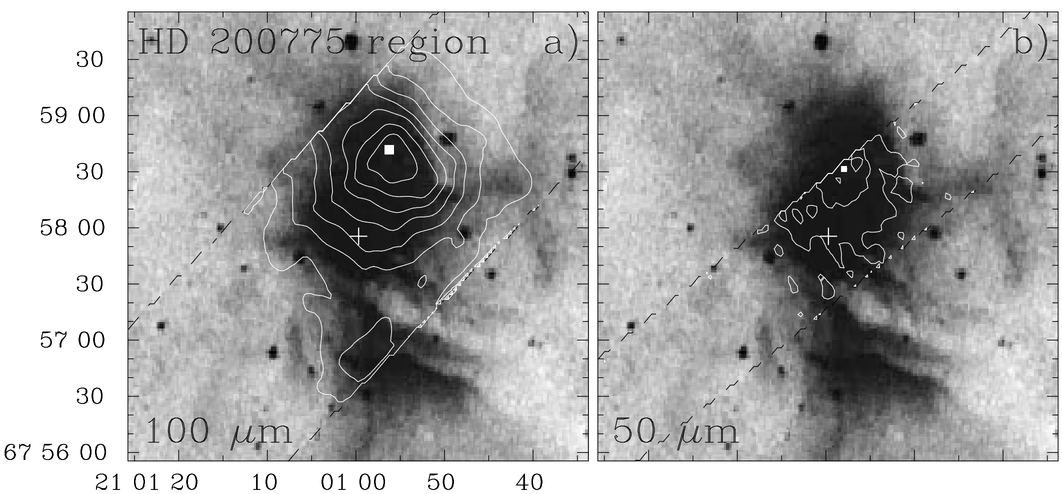

FIG. 8.—Far-infrared 2D maps of region containing HD 200775. See Fig. 1 for symbol/line definitions. (*a*) 100 μm 2D map with contours starting at and increasing in steps of 2 σ (27.5 Jy beam^{-1}) overlaid onto Digital Sky Survey image of region. (*b*) 50 μm 2D map with contours starting at and increasing in steps of 2 σ (69.3 Jy beam^{-1}) overlaid onto Digital Sky Survey image of region.

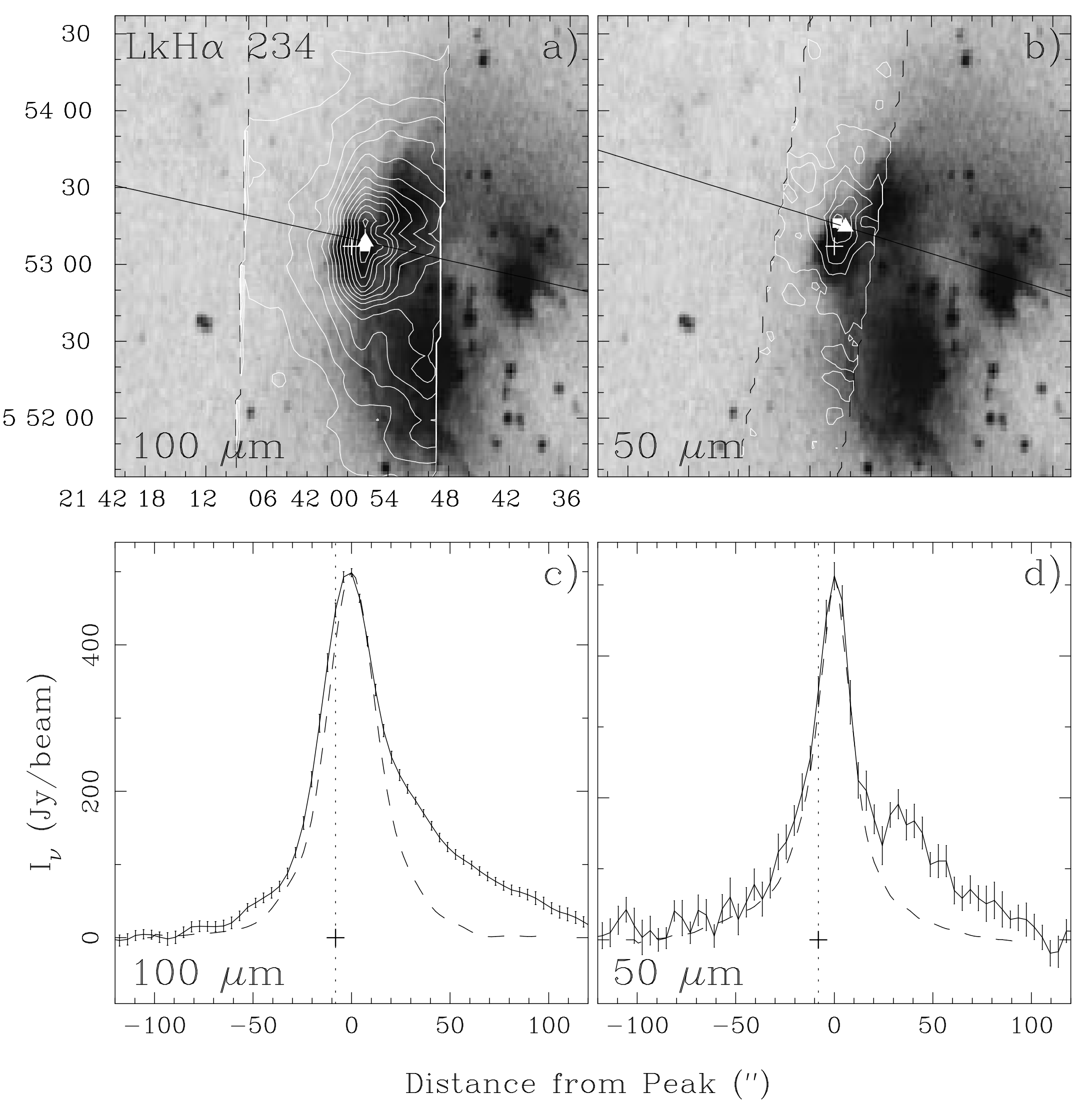

FIG. 9.—Far-infrared 2D and 1D maps of region containing LkHα 234. See Fig. 1 for symbol/line definitions. (*a*) 100 μm 2D map with contours starting at and increasing in steps of 2 σ (32.1 Jy beam^{-1}) overlaid onto Digital Sky Survey image of region. (*b*) 50 μm 2D map with contours starting at and increasing in steps of 2 σ (73.5 Jy beam^{-1}) overlaid onto Digital Sky Survey image of region. (*c*) 100 μm 1D profile with 1 σ error bars. (*d*) 50 μm 1D profile with 1 σ error bars.

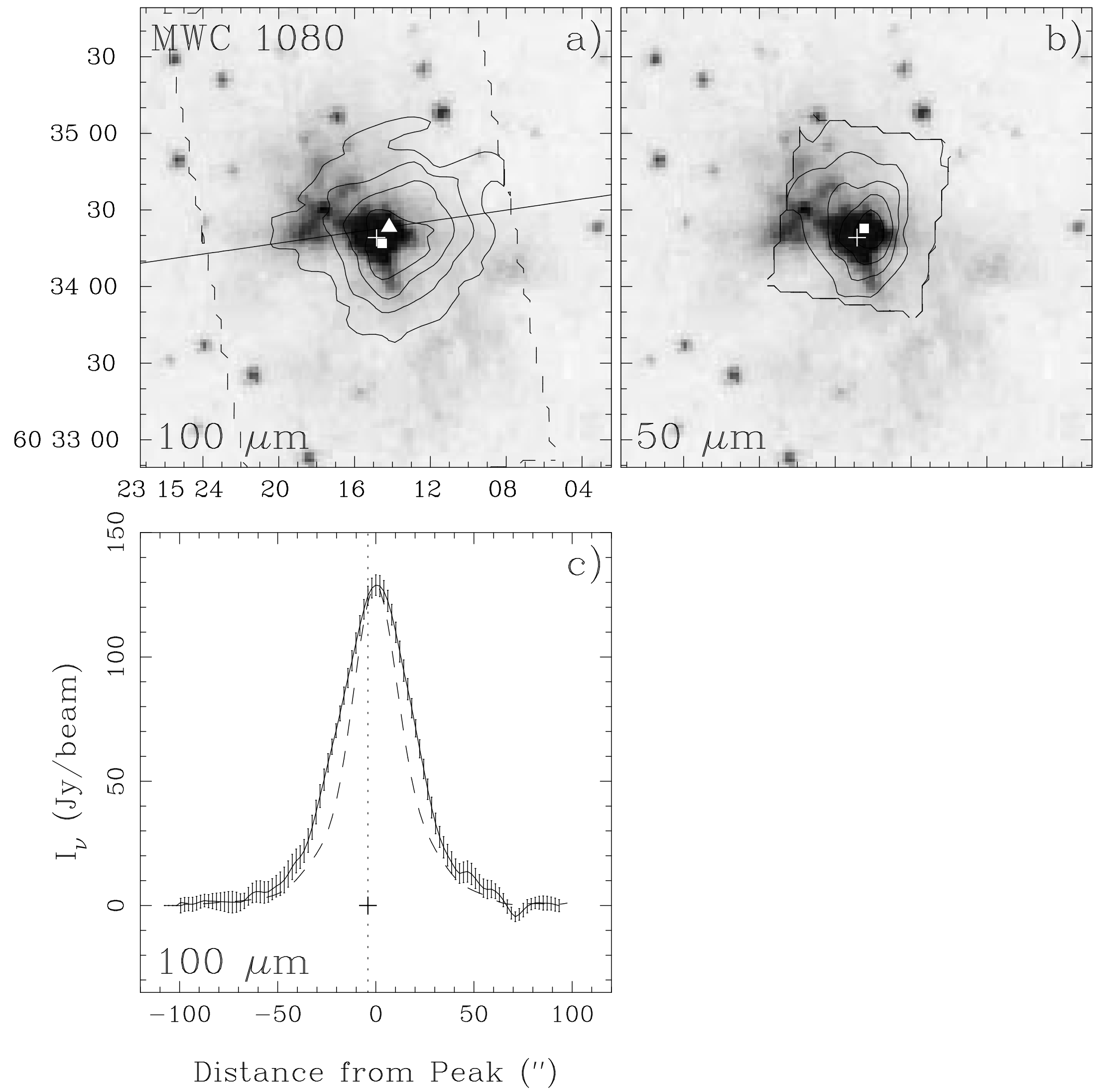

FIG. 10.—Far-infrared 2D and 1D maps of region containing MWC 1080. See Fig. 1 for symbol/line definitions. (*a*) 100 μm 2D map with contours starting at and increasing in steps of 2 σ (22.9 Jy beam^{-1}) overlaid onto Digital Sky Survey image of region. (*b*) 50 μm 2D map with contours starting at and increasing in steps of 2 σ (18.9 Jy beam^{-1}) overlaid onto Digital Sky Survey image of region. (*c*) 100 μm 1D profile with 1 σ error bars.

star, so the offset is definitely significant. Whitcomb et al. (1981) detected 55 and 125 μm emission (with 50″ resolution) at positions similar to our 100 μm peak. The increased resolution of our 100 μm maps confirms their observations that far-infrared emission in the NGC 7023 region is well displaced from HD 200775. Whitcomb et al. (1981) argued that the far-infrared emission is only due to a dust density enhancement northwest of HD 200775 heated externally by the optical star alone. No evidence for additional heating sources embedded within the enhancement were found by Whitcomb et al. (1981) from near-infrared imaging (limited to sources with $K < 9.4$) or mid-infrared imaging (limited to sources with $N < 2.5$). Recent images of the NGC 7023 region down to $K < 17$ by Testi, Palla, & Natta (1998) will likely further constrain this possibility (see § 4.3).

4.2. *Far-Infrared Spectral Energy Distributions*

Figures 23 and 24 show the SEDs of all objects where S_ν(KAO) at 100 μm was recovered. A good correspondence is found between S_ν(KAO) and S_ν(*IRAS*) at 100 μm and a slightly larger S_ν(KAO) at 50 μm is found relative to the overall infrared SEDs (see also § 3.4). Color-corrected S_ν(*IRAS*) at 12 and 25 μm are also shown with flux densities at 10 μm (*N* band) and 20 μm (*Q* band) obtained by Hillenbrand et al. (1992) on the optical positions of the Herbig Ae/Be stars. The *N*-band and *Q*-band observations were made with apertures ranging from 6″ to 12″ in size, and therefore reflect the mid-infrared emission in close proximity to the optical positions, as opposed to *IRAS* flux densities that reflect emission within the much larger *IRAS* beams (i.e., $\sim$120″ at 100 μm). Several sources in Figure 23 (Herbig Ae/Be stars) show distinct differences between these sets of flux densities, which were explained by Hillenbrand et al. (1992) as possibly due to transiently heated dust or other sources within the *IRAS* beam(s).

Single far-infrared sources are overwhelmingly found in our 100 μm maps of these regions, with general consistency between 100 μm flux densities, at times significantly displaced from the optical positions of the Herbig Ae/Be stars. Figure 25 shows how the ratios of the ground-based to *IRAS*-flux densities at both $\sim$10 (Fig. 25*a*) and $\sim$20 μm

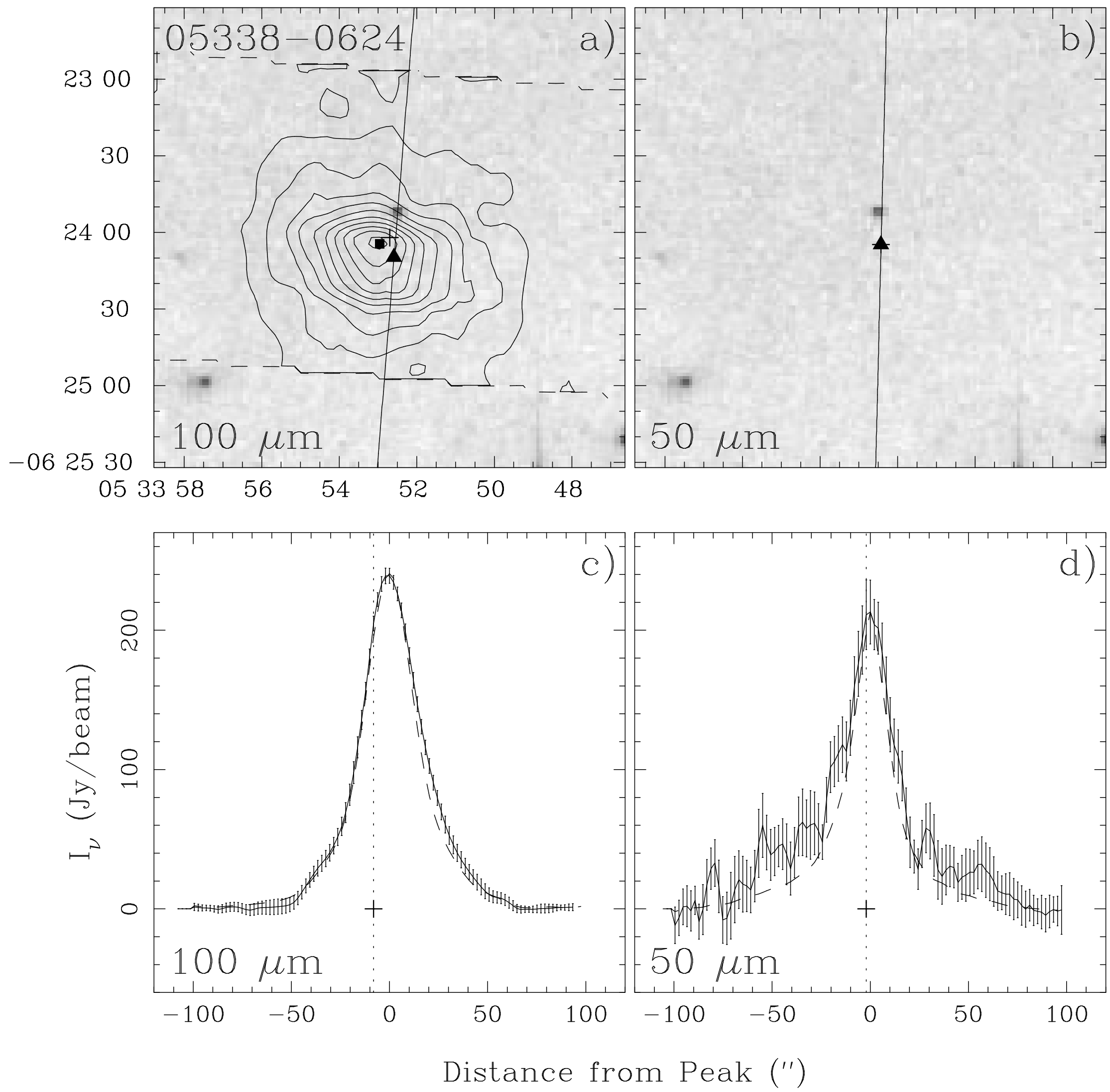

FIG. 11.—Far-infrared 2D and 1D maps of region containing *IRAS* 05338−0624. See Fig. 1 for symbol/line definitions. (*a*) 100 μm 2D map with contours starting at and increasing in steps of 2 σ (23.8 Jy beam^{-1}) overlaid onto Digital Sky Survey image of region. (*b*) Position of 50 μm 1D map overlaid onto Digital Sky Survey image of region. (*c*) 100 μm 1D profile with 1 σ error bars. (*d*) 50 μm 1D profile with 1 σ error bars.

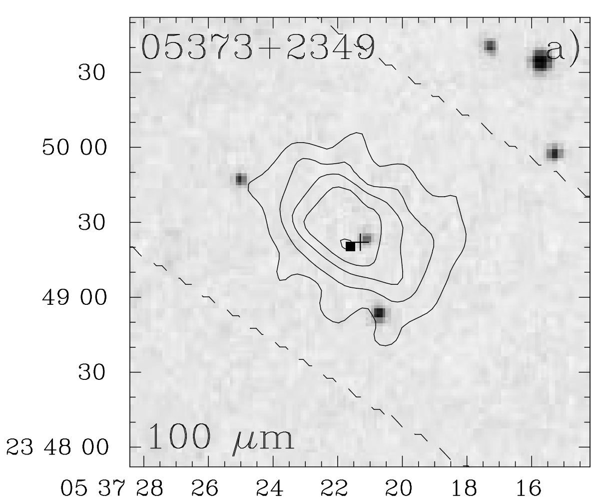

FIG. 12.—Far-infrared 2D map of region containing *IRAS* 05373+2349 (see Fig. 1 for symbol/line definitions); 100 μm 2D map with contours starting at and increasing in steps of 2 σ (32.4 Jy beam^{-1}) overlaid onto Digital Sky Survey image of region.

(Fig. 25*b*) decrease with the measured offset between optical position and far-infrared (KAO) peak position. (A similar trend is seen with *IRAS* PSC positions; see Figs. 25*c* and 25*d*.) For Elias 3-1, AB Aur, and MWC 1080, both sets of mid-infrared flux densities appear consistent, and their small far-infrared offsets indicate they are probably immediately surrounded by far-infrared emitting dust. For the remaining sources, all with larger far-infrared offsets, the mid-infrared *IRAS* flux densities may be associated with dust spatially distinct from the Herbig Ae/Be stars. These results further suggest that far-infrared emitting dust may not immediately surround Herbig Ae/Be stars in all cases (see § 2.3).

4.3. *Deconvolved Sizes and Shapes of Far-Infrared Sources*

The detected sources in our 2D and 1D maps have been deconvolved assuming Gaussian beam shapes to estimate the intrinsic linear sizes and shapes of the emitting areas at far-infrared wavelengths. Maps in 2D were deconvolved using the task IMFIT in AIPS, which include position angles of the source and the beam. Maps in 1D were decon-

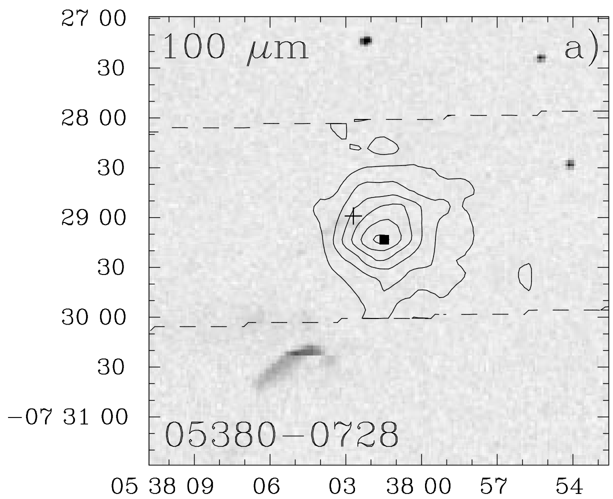

FIG. 13.—Far-infrared 2D map of region containing *IRAS* 05380−0728 (see Fig. 1 for symbol/line definitions); 100 μm 2D map with contours starting at and increasing in steps of 2 σ (18.2 Jy beam^{-1}) overlaid onto Digital Sky Survey image of region.

volved using a straightforward 1D Gaussian method; i.e., $(\mathrm{FWHM_{decon}})^2 = (\mathrm{FWHM_{obj}})^2 - (\mathrm{FWHM_{calib}})^2$. Linear sizes were then estimated using the distances to each source listed in Table 1. The deconvolved sizes (and aspect ratios from 2D maps, where applicable) of each source are listed in Table 5. Following § 4.1, far-infrared emission in the BD +40°4124 or HD 200775 regions does not originate from areas immediately surrounding the stars themselves.

Geometrical means of the deconvolved 2D sizes in Table 5 were calculated to facilitate comparisons. From these geometrical means, we find the mean deconvolved size (and standard deviation) of resolved objects in Herbig Ae/Be regions at 100 μm is 0.22 ± 0.14 pc (from the 2D maps of six objects; the unresolved AB Aur object, and the BD +40°4124/V1686 Cyg, and HD 200775 objects were not included). In comparison, the mean deconvolved size (and standard deviation) of the resolved embedded *IRAS* objects is only 0.12 ± 0.06 pc (from the 2D maps of seven objects), less than the mean size of the Herbig Ae/Be region objects. However, this Herbig region subsample includes very luminous objects at distances greater than 1.0 kpc, while the embedded regions subsample has no objects greater than this distance. Removing sources more distant than 1.0 kpc from the Herbig Ae/Be region subsample, the mean deconvolved size (and standard deviation) of resolved objects in Herbig Ae/Be regions at 100 μm reduces to 0.15 ± 0.10 pc, very consistent with the mean deconvolved size of the resolved embedded *IRAS* object subsample. At 50 μm, the mean deconvolved sizes determined from 2D maps of each subsample are very consistent despite the small numbers; 0.10 ± 0.01 pc for two Herbig Ae/Be sample objects, and 0.14 ± 0.06 pc for three embedded sample objects. Mean sizes from 1D maps at both 100 and 50 μm were also consistent with those obtained from 2D maps. No significant difference is found between far-infrared sizes of objects in each subsample considered. (Including the BD +40°4124 and HD 200775 region objects in these analyses does not affect our conclusions.) The sizes are similar to those of regions forming low-mass stars. They are characteristic of envelopes around forming stars and are far larger than the expected sizes of disks.

A possible difference is found in the shapes of the far-infrared objects in each subsample. The aspect ratios (i.e., ratio of major to minor axis) of deconvolved objects show the embedded *IRAS* sample is more flattened as a population than those far-infrared objects that immediately surround Herbig Ae/Be stars (i.e., excluding the BD +40°4124 and HD 200775 region objects). For example, the deconvolved sizes of six of seven embedded *IRAS* objects in 2D 100 μm maps (and two of three objects in 2D 50 μm maps) have aspect ratios that are significantly larger than expected for circular sources (i.e, the aspect ratios are greater than 1 σ from 1.0), which suggests significant flattening. In contrast, only two of six objects in Herbig Ae/Be regions in 2D 100 μm maps and zero of three objects in 2D 50 μm maps (again excluding the BD +40°4124 and HD 200775 objects) have aspect ratios significantly larger than 1.0 when deconvolved. This dichotomy may be because the uncertainties in the aspect ratios of the Herbig subsample are slightly larger on average than those of the embedded subsample. For example, the mean uncertainty of the aspect ratios of the 2D 100 μm maps of seven embedded *IRAS* objects is 0.22, but

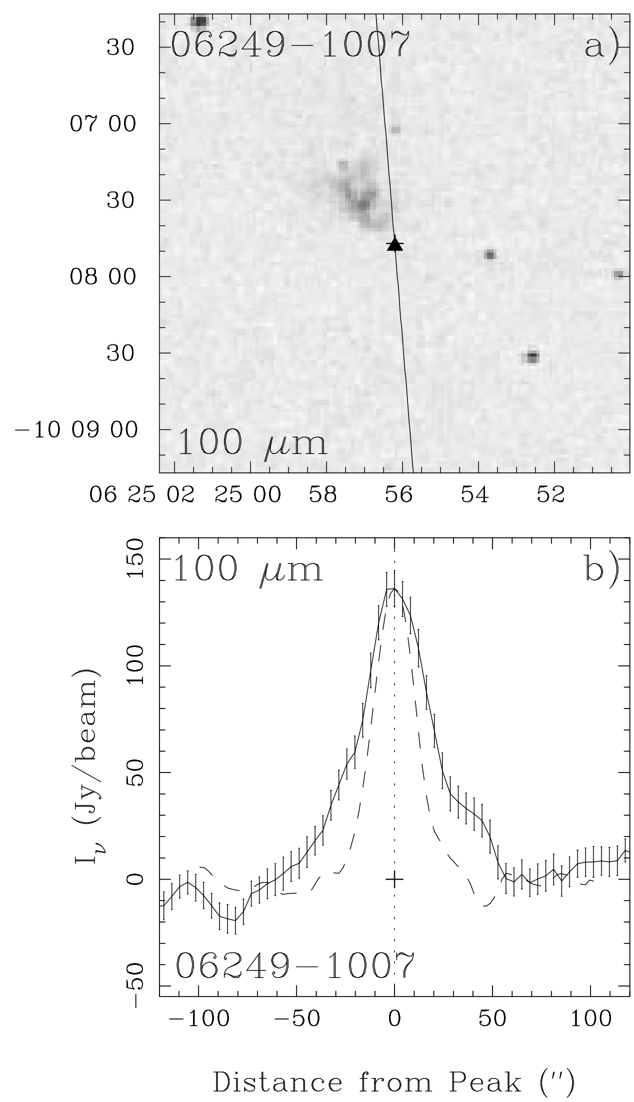

FIG. 14.—Far-infrared 1D map of region containing *IRAS* 06249−1007. See Fig. 1 for symbol/line definitions. (*a*) Position of 100 μm 1D map overlaid onto Digital Sky Survey image of region. (*b*) 100 μm 1D profile with 1 σ error bars. Coordinates are relative to the peak intensity located at $\alpha(1950.0) = 06^{\mathrm{h}}24^{\mathrm{m}}56\overset{\mathrm{s}}{.}2$, $\delta(1950.0) = -10°07'48''$.

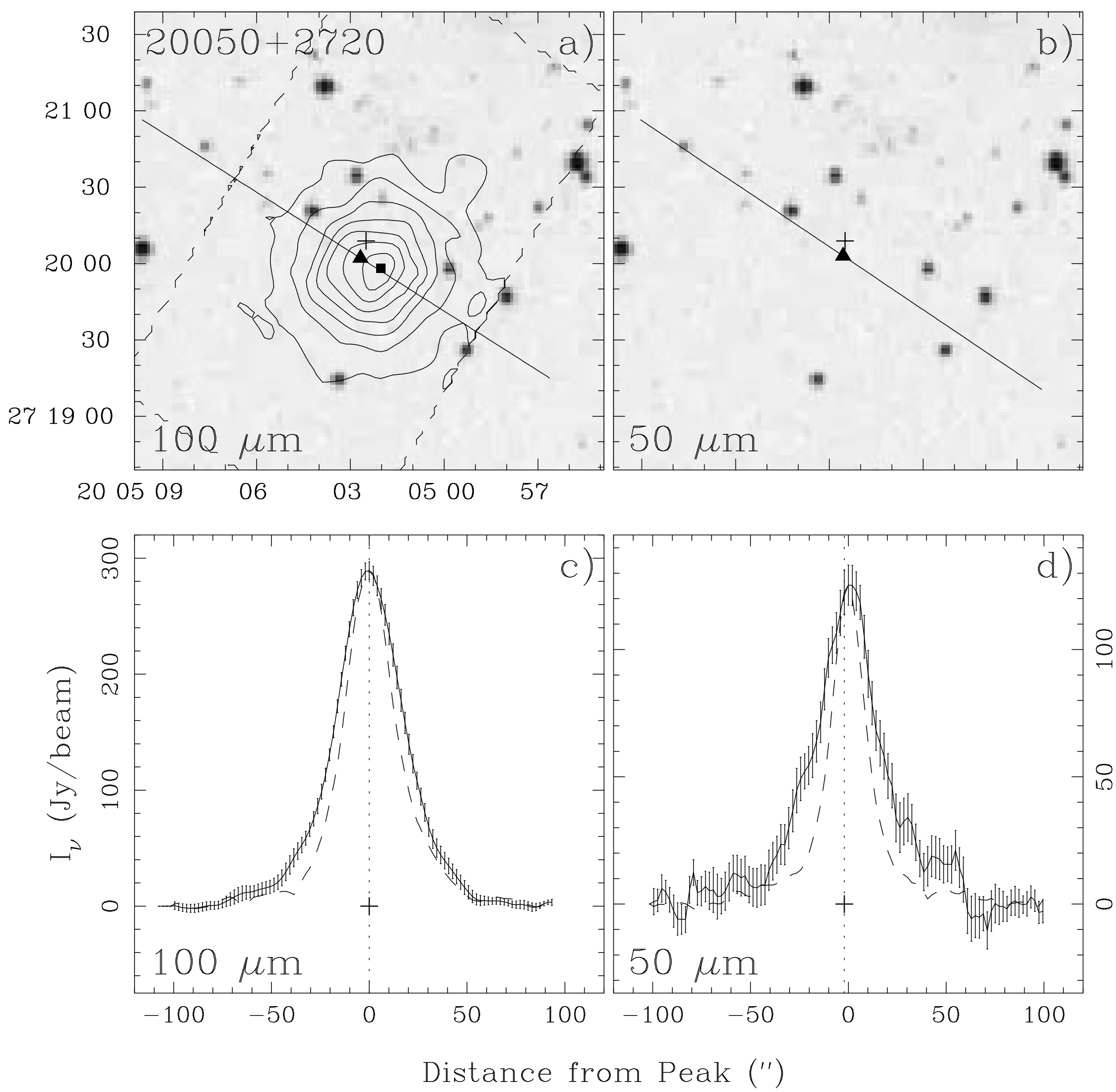

FIG. 15.—Far-infrared 2D and 1D maps of region containing *IRAS* 20050+2720. See Fig. 1 for symbol/line definitions. (*a*) 100 μm 2D map with contours starting at and increasing in steps of 2 σ (38.3 Jy beam^{-1}) overlaid onto Digital Sky Survey image of region. (*b*) Position of 50 μm 1D map overlaid onto Digital Sky Survey image of region. (*c*) 100 μm 1D profile with 1 σ error bars. (*d*) 50 μm 1D profile with 1 σ error bars.

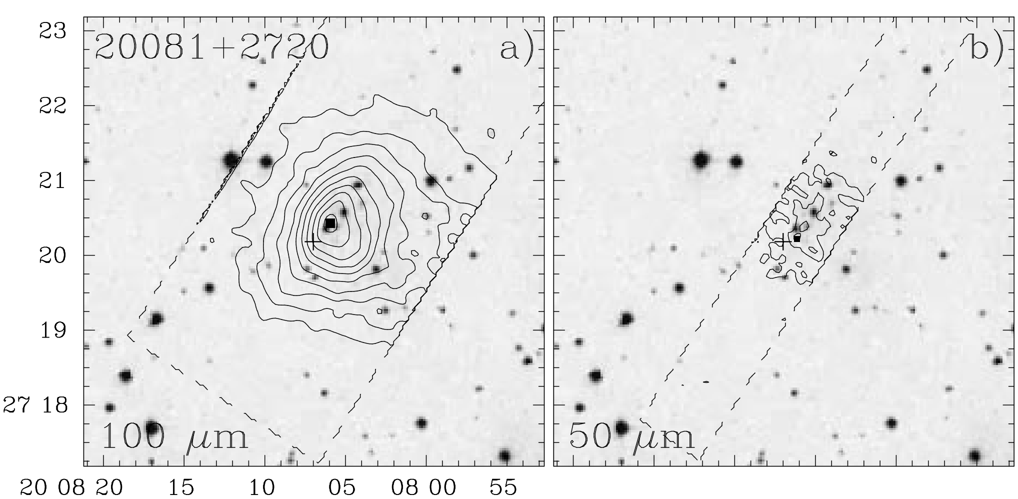

FIG. 16.—Far-infrared 2D and 1D maps of region containing *IRAS* 20081+2720. See Fig. 1 for symbol/line definitions. (*a*) 100 μm 2D map with contours starting at and increasing in steps of 2 σ (29.0 Jy beam^{-1}) overlaid onto Digital Sky Survey image of region. (*b*) 50 μm 2D map with contours starting at and increasing in steps of 2 σ (73.5 Jy beam^{-1}) overlaid onto Digital Sky Survey image of region.

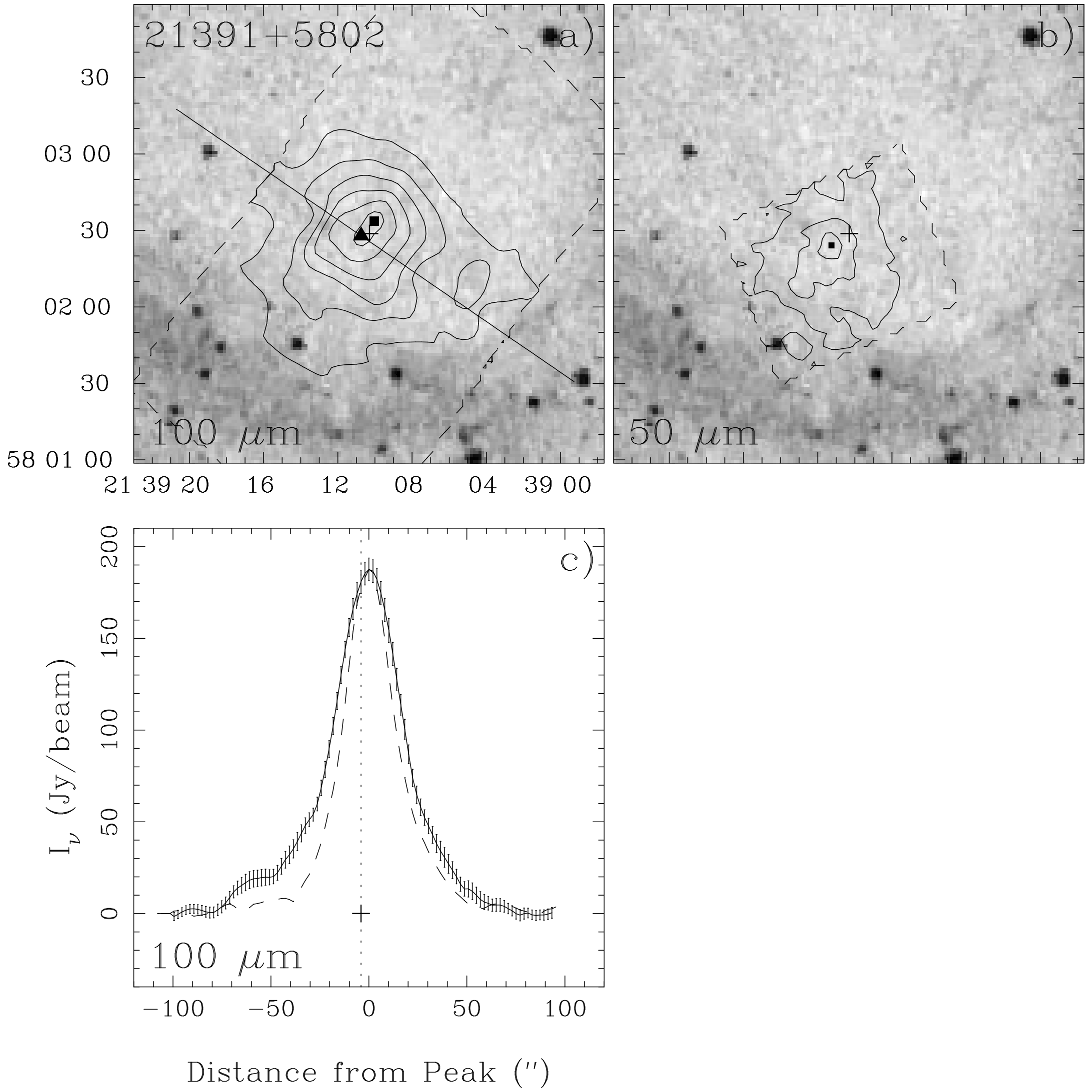

FIG. 17.—Far-infrared 2D and 1D maps of region containing *IRAS* 21391 + 5802. See Fig. 1 for symbol/line definitions. (*a*) 100 μm 2D map with contours starting at and increasing in steps of 2 σ (30.2 Jy beam^{-1}) overlaid onto Digital Sky Survey image of region. (*b*) 50 μm 2D map with contours starting at and increasing in steps of 2 σ (31.5 Jy beam^{-1}) overlaid onto Digital Sky Survey image of region. (*c*) 100 μm 1D profile with 1 σ error bars.

for five Herbig region objects (excluding Elias 3-1) the mean uncertainty is 0.35. Therefore, objects in the embedded sample could be more easily identified as "flattened" because of their smaller uncertainties.

An alternative explanation of the dichotomy between shapes of the subsamples could be that an envelope morphology is common to objects of both subsamples but is viewed preferentially from different orientations. In this scenario, the far-infrared objects associated with sources in both subsamples may be envelopes flattened during collapse, but envelopes around Herbig Ae/Be stars are then seen preferentially "pole-on," along their axes of symmetry, while envelopes around embedded *IRAS* objects are seen preferentially "edge-on," along their equators. Pole-on envelopes would appear more circular than the flattened, ellipsoidal edge-on envelopes, as observed. Given the reduced optical depths expected along the poles of flattened envelopes and the increased optical depths expected along their equators (see, e.g., Kenyon, Calvet, & Hartmann 1993), Herbig Ae/Be stars may be visible only due to a fortuitous pole-on orientation of their envelopes with respect to us, while embedded sources remain invisible due to their edge-on oriented envelopes. (Of the two far-infrared objects spatially distinct from nearby Herbig Ae/Be stars that could contain separate, more embedded objects, the HD 200775 object is significantly flattened but the BD +40°4124 object, likely containing V1318 Cyg, is not.) A common flattened morphology for envelopes of both types of intermediate-mass young stellar objects suggests their differences may be related less strictly to evolution than previously assumed (see W89). In addition, these deconvolved shapes suggest the spherically symmetrical envelopes assumed previously for earlier models of intermediate-mass objects (see, e.g., Natta et al. 1993) may not be applicable here.

Finally, the relative sizes of far-infrared emission at 100 and 50 μm are surprisingly similar, assuming a centrally heated envelope by a single object. From objects where 2D maps at both wavelengths were available (i.e., four objects in Herbig Ae/Be regions, three objects in embedded *IRAS* regions), the ratio of deconvolved size at 100 to 50 μm is 1.05 ± 0.30 (standard deviation) for objects in Herbig Ae/Be

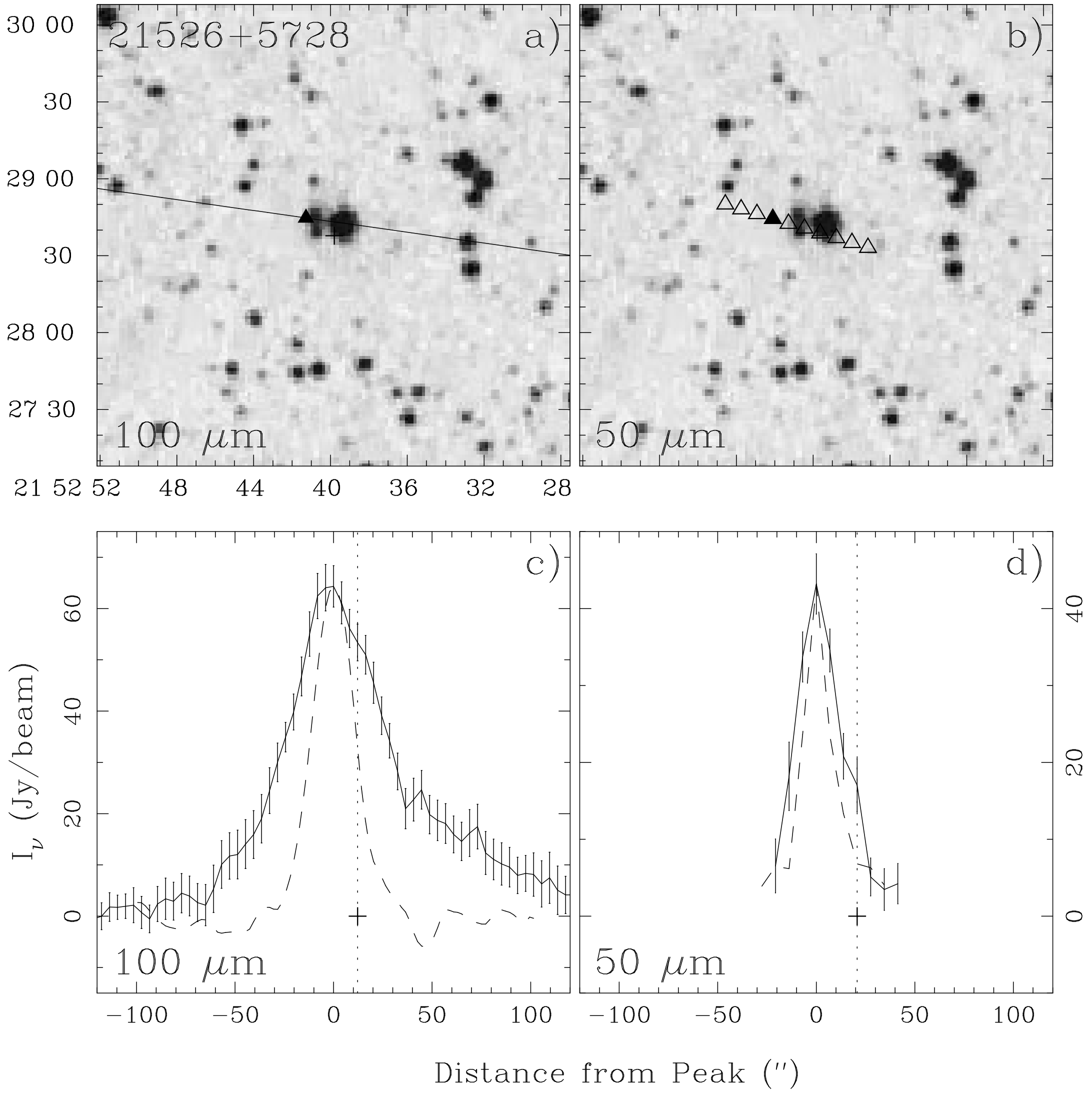

FIG. 18.—Far-infrared 1D maps of region containing *IRAS* 21526+5728. See Fig. 1 for symbol/line definitions, but note that open triangles here denote positions of individual detectors in 1D stare-mode maps. (*a*) Positions of 1D 100 μm map overlaid onto Digital Sky Survey image of region. (*b*) Positions of 1D 50 μm map overlaid onto Digital Sky Survey image of region. (*c*) 100 μm 1D profile with 1 σ error bars. Coordinates are relative to the position of peak intensity located at $\alpha(1950.0) = 21^h52^m41^s.3$, $\delta(1950.0) = +57°28'45''$. (*d*) 50 μm 1D profile with 1 σ error bars. Coordinates are relative to the position of peak intensity located at $\alpha(1950.0) = 21^h52^m42^s.1$, $\delta(1950.0) = +57°28'44''$.

regions, and 1.15 ± 0.27 (standard deviation) for objects in embedded *IRAS* regions. (Similar ratios near 1.0 are found when comparing deconvolved 1D maps at both wavelengths.) In several instances, the 50 μm deconvolved size is larger than its 100 μm counterpart. The envelopes may be heated by a distribution (e.g., a cluster) of fairly luminous sources, rather than the single very luminous source assumed in recent models of other intermediate-mass sources (see Natta et al. 1993 or Butner & Natta 1995). For example, a sizable embedded cluster of objects near *IRAS* 20050+2720 was detected recently by Chen et al. (1997). In addition, Testi et al. (1997) (see also Testi et al. 1998) show that the degree of clustering of near-infrared objects is strongest around Herbig stars of B7 spectral type and earlier. To determine the effect young clusters have on the far-infrared emission observed in these regions, recent near-infrared images, e.g., those of Testi et al. (1997), must be analyzed to compare the positions of highly embedded, luminous sources (if they exist) with the extent of far-infrared emission in each region.

5. SUMMARY

High-resolution far-infrared 2D and/or 1D maps have been obtained for 19 regions containing 20 intermediate-mass objects with a scanning photometer system and the KAO. The observed sample included 10 Herbig Ae/Be stars and 10 intermediate-luminosity, highly embedded *IRAS* point sources. In most cases, a single source was detected in each map at 100 μm, and at 50 μm if available. All embedded *IRAS* sources are found to peak within a half–KAO beamwidth of the positions expected from the *IRAS* PSC. The situation is more ambiguous for sources in regions containing Herbig Ae/Be stars, with only six of 10 objects peaking within one half–KAO beamwidth of positions listed in the Herbig-Bell Catalog. Almost all sources are extended with respect to the KAO resolution at both 100 and 50 μm (if available). Only sources associated with AB Aur and possibly *IRAS* 05338−0624 are unresolved at both wavelengths. Derived flux densities for all sources at 100 μm are quite consistent with *IRAS* flux densities,

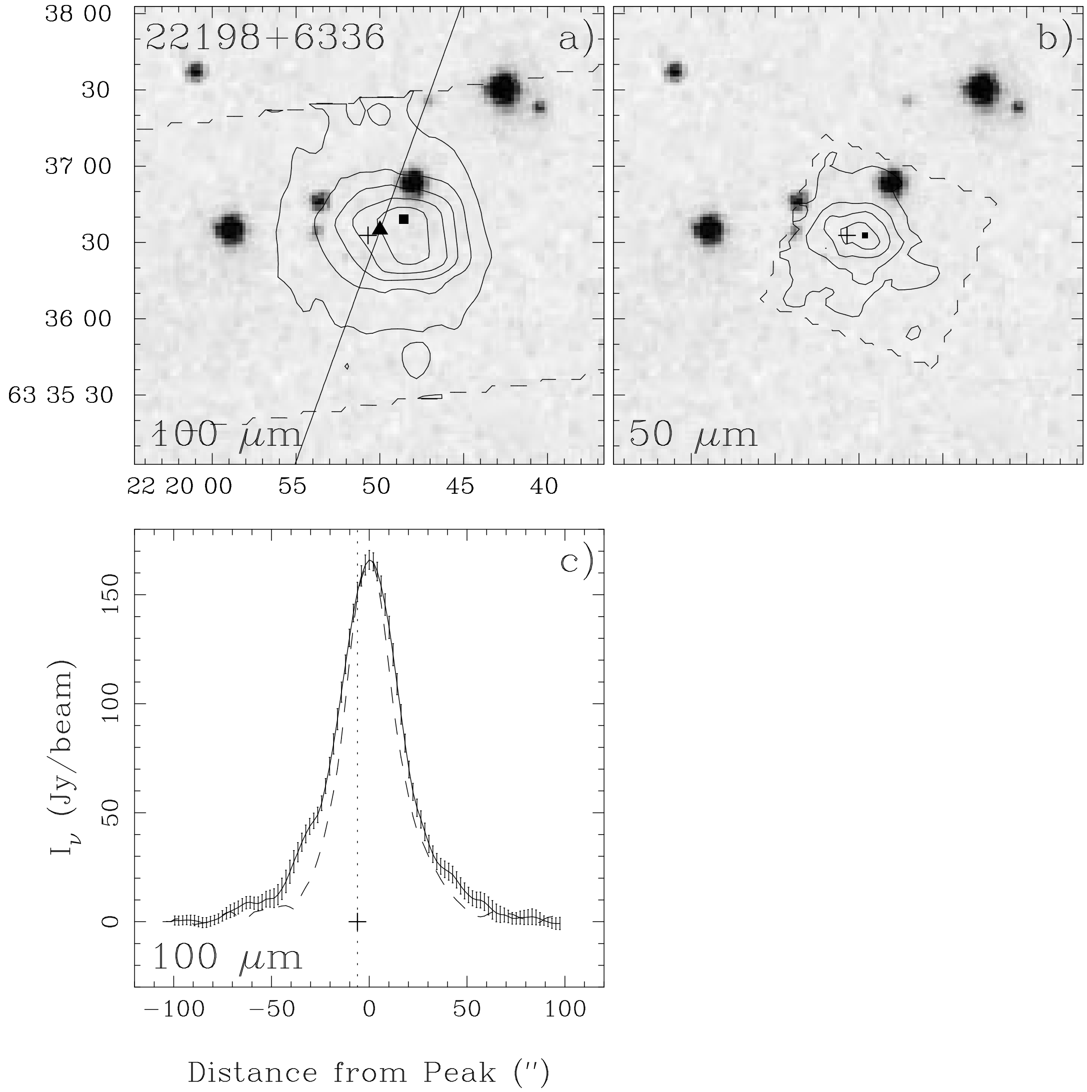

FIG. 19.—Far-infrared 2D and 1D maps of region containing *IRAS* 22198+6336. See Fig. 1 for symbol/line definitions. (*a*) 100 μm 2D map with contours starting at and increasing in steps of 2 σ (28.9 Jy beam^{-1}) overlaid onto Digital Sky Survey image of region. (*b*) 50 μm 2D map with contours starting at and increasing in steps of 2 σ (27.7 Jy beam^{-1}) overlaid onto Digital Sky Survey image of region. (*c*) 100 μm 1D profile with 1 σ error bars.

although derived flux densities at 50 μm are larger than expected given the *IRAS* mid- to far-infrared SEDs. These maps can provide excellent independent spatial constraints on envelope models of pre–main-sequence circumstellar environments.

The displacements of peaks of far-infrared emission from the optical positions of some Herbig Ae/Be stars are larger than expected, given similar observations of the embedded *IRAS* subsample. Also, the differences between ground-based and *IRAS* mid-infrared photometry of Herbig Ae/Be stars increase with these displacements. Together, these points suggest that the far-infrared emission may not originate from regions immediately surrounding the Herbig Ae/Be stars in all cases. Instead, nearby density enhancements, either heated externally by the Herbig stars or internally by highly embedded sources, may be producing the bulk of far-infrared emission, which has been previously attributed to a disk and/or envelope surrounding the Herbig Ae/Be stars. This is very apparent for cases like the HD 200775 object; the same may be true for cases like AB Aur or MWC 1080 where the superposition of optical and far-infrared emission is merely coincidental.

Estimated far-infrared sizes of objects in both subsamples are quite similar at both wavelengths, but a comparison of their shapes reveals that sources in the embedded *IRAS* subsample may be generally flatter than those immediately associated with Herbig Ae/Be stars. The difference between sources in our subsamples could be merely a matter of orientation; a flattened envelope structure common to objects of both subsamples, but viewed from different angles, may account for this behavior. Finally, the relatively similar sizes of emission at 100 and 50 μm suggest the envelopes may have multiple, rather than singular, sources of heating. Recent sensitive, near-infrared images of these regions must be analyzed to determine if nearby highly embedded luminous sources are found at positions more consistent with that of far-infrared emission than the optical sources. If the inferences drawn from our far-infrared data are valid, previous models of intermediate-mass sources, which assumed spherically symmetric envelopes surrounding a solitary luminous source, are likely inapplicable to these objects.

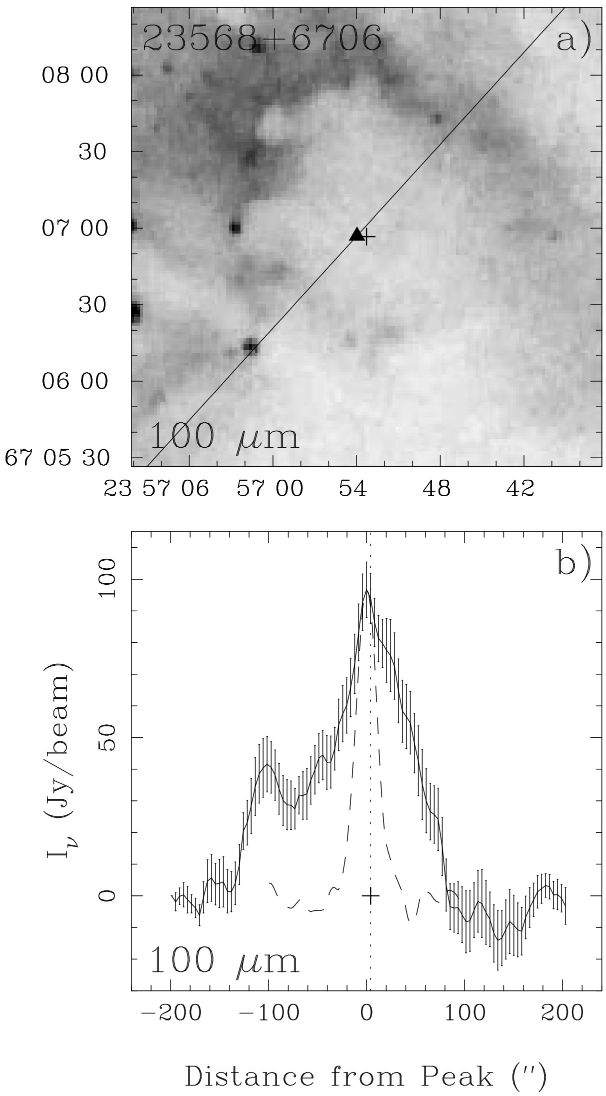

FIG. 20.—Far-infrared 1D maps of region containing *IRAS* 23568+6706. (*a*) Position of 100 μm 1D map overlaid onto Digital Sky Survey image of region. (*b*) 100 μm 1D profile with 1 σ error bars. Coordinates are relative to the position of peak intensity at $\alpha(1950.0) = 23^{\mathrm{h}}56^{\mathrm{m}}53\overset{\mathrm{s}}{.}9$, $\delta(1950.0) = +67°06'57''$. The range in coordinates is doubled with respect to 1D profiles in other figures.

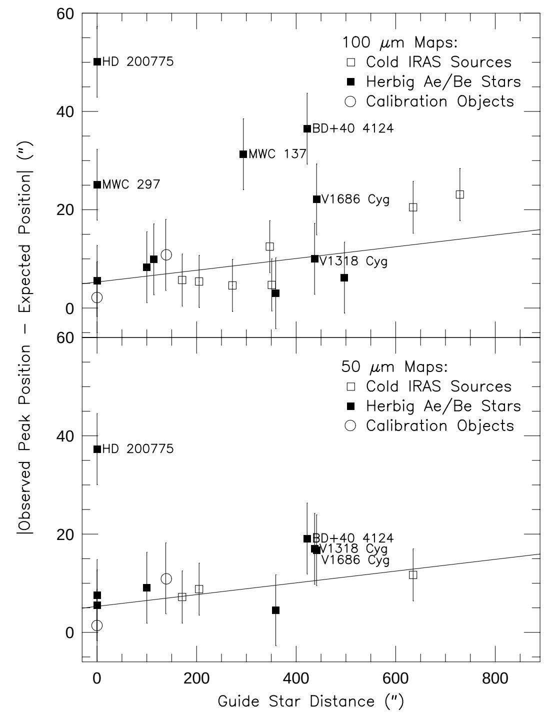

FIG. 21.—Positional offsets of observed peaks in 2D KAO maps from expected positions vs. positional offsets from guide stars used in observations (GSD). Circles indicate offsets from expected positions of calibration objects (see Table 2). Open squares indicate offsets from expected positions of embedded *IRAS* objects (see Table 4). Filled squares indicate offsets from expected positions of Herbig Ae/Be stars (see Table 4). Error bars are estimates of intrinsic pointing uncertainty from calibration objects with zero GSD. Solid lines are least-square fits to the calibration and embedded *IRAS* object sample (see text).

This work has been supported by NASA grants NAG 2-420 and 2-1055. We thank Allan Meyer, Bev Smith, Cecilia Colomé, Tim Jenness, Tom Chester, Lee Hartmann, and Nuria Calvet for their assistance during the writing of this paper. Several years of excellent support provided by the staff of the Kuiper Airborne Observatory is gratefully acknowledged. This research made use of the SIMBAD database, operated at CDS, Strasbourg, France.

TABLE 4

EXPECTED AND OBSERVED PEAK POSITIONS OF HERBIG AE/BE OBJECTS

Source Name	λ (μm)	Scan Type	Expected R.A.	Expected Decl.	Measured R.A.	Measured Decl.	Offset (arcsec)
Elias 3-1	100	2D	04 15 34.51	+28 12 01.8	04 15 34.85	+28 12 06.2	6.2
	50	1D	04 15 34.51	+28 12 01.8	04 15 34.27	+28 12 08.8	7.7
AB Aur	100	2D	04 52 34.24	+30 28 21.9	04 52 34.51	+30 28 17.7	5.5
	100	1D	04 52 34.24	+30 28 21.9	04 52 34.48	+30 28 19.2	4.1
	50	2D	04 52 34.24	+30 28 21.9	04 52 34.37	+30 28 14.5	7.6
MWC 137	100	2D	06 15 53.51	+15 18 09.1	06 15 53.75	+15 17 38.0	31.3
	100	1D	06 15 53.51	+15 18 09.1	06 15 53.64	+15 17 56.2	13.0
	50	2D	06 15 53.51	+15 18 09.1	06 15 52.68	+15 17 54.3	19.0
	50	1D	06 15 53.51	+15 18 09.1	06 15 53.74	+15 18 06.4	4.3
LkHa 215	100	2D	06 29 56.1	+10 11 24	06 29 56.28	+10 11 33.6	9.9
	100	1D	06 29 56.1	+10 11 24	06 29 56.02	+10 11 50.0	26.0
MWC 297	100	2D	18 25 01.22	−03 51 46.3	18 25 02.69	−03 51 34.2	25.1
	100	1D	18 25 01.22	−03 51 46.3	18 25 01.58	−03 51 36.1	11.5
	50	2D	18 25 01.22	−03 51 46.3	18 25 00.90	−03 51 43.5	5.5
	50	1D	18 25 01.22	−03 51 46.3	18 25 01.15	−03 51 51.3	5.2
BD+40 4124......	100	2D	20 18 42.7	+41 12 18	20 18 45.51	+41 12 00.0	36.5
	50	2D	20 18 42.7	+41 12 18	20 18 44.22	+41 12 09.6	19.1
HD 200775........	100	2D	21 00 59.7	+67 57 55.5	21 00 56.22	+67 58 41.6	50.1
	50	2D	21 00 59.7	+67 57 55.5	21 00 57.95	+67 58 31.4	37.3
LkHa 234	100	2D	21 41 57.60	+65 53 07.1	21 41 56.24	+65 53 06.9	8.3
	100	1D	21 41 57.60	+65 53 07.1	21 41 56.22	+65 53 08.8	8.6
	50	2D	21 41 57.60	+65 53 07.1	21 41 57.32	+65 53 16.1	9.1
	50	1D	21 41 57.60	+65 53 07.1	21 41 56.50	+65 53 14.7	10.1
MWC 1080........	100	2D	23 15 14.84	+60 34 19.2	23 15 14.55	+60 34 17.0	3.0
	100	1D	23 15 14.84	+60 34 19.2	23 15 14.18	+60 34 23.3	6.4
	50	2D	23 15 14.84	+60 34 19.2	23 15 14.47	+60 34 22.7	4.5
05338−0624	100	2D	05 33 52.70	−06 24 02.0	05 33 52.96	−06 24 04.6	4.7
	100	1D	05 33 52.70	−06 24 02.0	05 33 52.58	−06 24 09.7	7.9
	50	1D	05 33 52.70	−06 24 02.0	05 33 52.43	−06 24 04.7	4.9
05373+2349	100	2D	05 37 21.30	+23 49 22.0	05 37 21.61	23 49 20.3	4.6
05380−0728	100	2D	05 38 02.70	−07 28 59.0	05 38 01.48	−07 29 13.3	23.1
06249−1007	100	1D	06 24 56.20	−10 07 47.0	06 24 56.20	−10 07 48.0	1.0
20050+2720	100	2D	20 05 02.50	+27 20 08.9	20 05 02.02	+27 19 58.2	12.5
	100	1D	20 05 02.50	+27 20 08.9	20 05 02.68	+27 20 02.2	7.1
	50	1D	20 05 02.50	+27 20 08.9	20 05 02.56	+27 20 03.0	6.0
20081+2720	100	2D	20 08 07.00	+27 20 10.9	20 08 05.96	+27 20 25.9	20.5
	50	2D	20 08 07.00	+27 20 10.9	20 08 06.14	+27 20 13.2	11.7
21391+5802	100	2D	21 39 10.30	+58 02 28.8	21 39 10.03	+58 02 33.7	5.4
	100	1D	21 39 10.30	+58 02 28.8	21 39 10.75	+58 02 27.9	3.6
	50	2D	21 39 10.30	+58 02 28.8	21 39 11.25	+58 02 24.2	8.8
21526+5728	100	1D	21 52 39.80	+57 28 37.8	21 52 41.27	+57 28 44.7	13.7
	50	1D	21 52 39.80	+57 28 37.8	21 52 42.10	+57 28 44.5	19.8
22198+6336	100	2D	22 19 50.71	+63 36 32.8	22 19 48.56	+63 36 39.2	5.7
	100	1D	22 19 50.71	+63 36 32.8	22 19 49.99	+63 36 35.0	5.3
	50	2D	22 19 50.71	+63 36 32.8	22 19 49.62	+63 36 32.7	7.2
23568+6706	100	1D	23 56 53.29	+67 06 56.7	23 56 53.98	+67 06 57.0	4.0

NOTE.—Units of right ascension are hours, minutes, and seconds, and units of declination are degrees, arcminutes, and arcseconds.

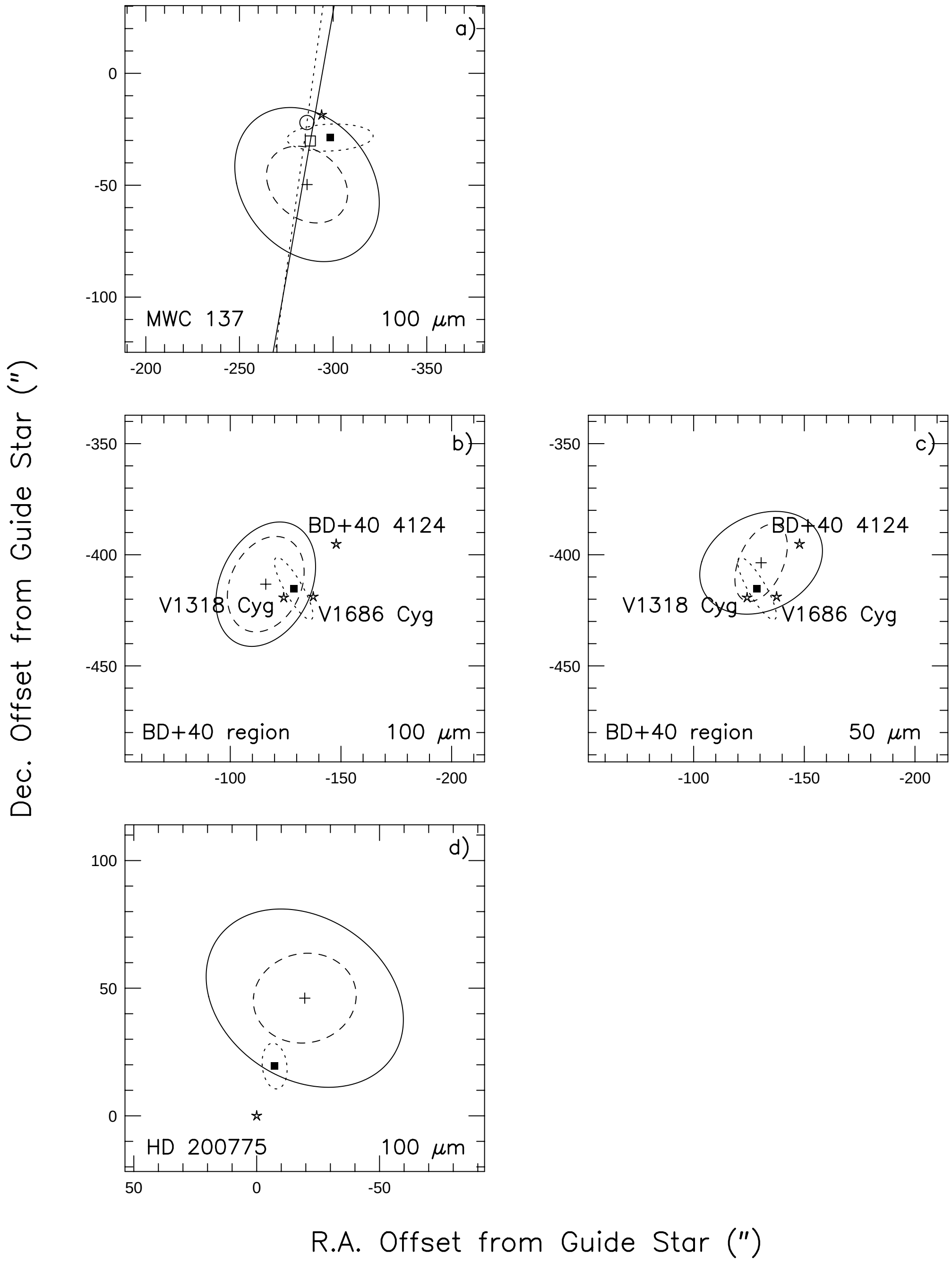

FIG. 22.—Relative positions of optical source (*star*), *IRAS* point source (*filled square*), and object in KAO map (*cross*) for selected cases to the guide star. *IRAS* positional uncertainties are indicated by dotted ellipses. Solid ellipses are the measured FWHM of the detected KAO object, and dashed ellipses are the beam size and shape centered at positions of peak intensity. For the MWC 137 region at 100 μm, relative positions of the KAO 100 μm 1D profile (*solid line*) and peak (*open square*) and the KAO 50 μm 1D profile (*dotted line*) and peak (*circle*) are also shown.

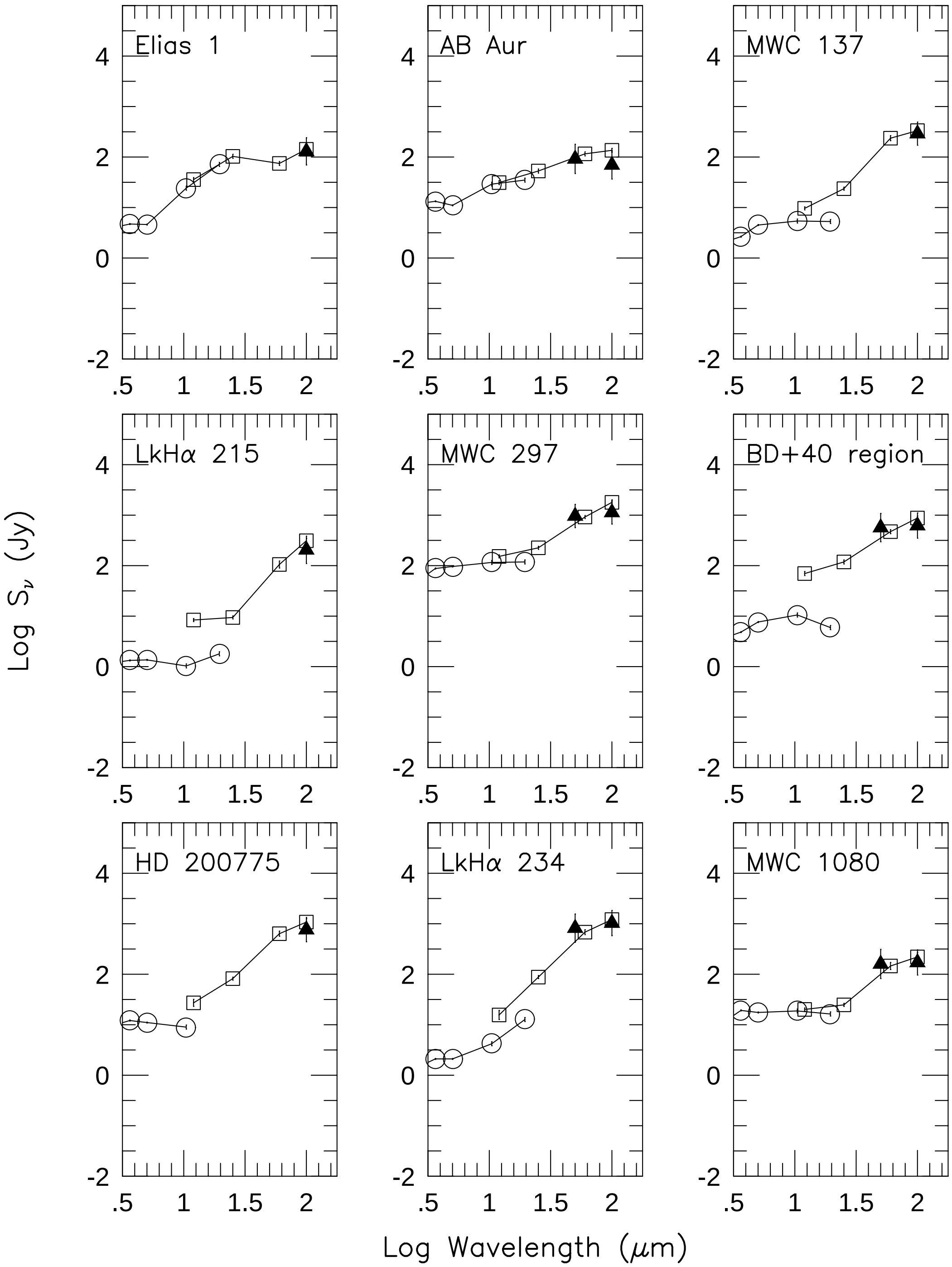

FIG. 23.—Infrared spectral energy distributions for selected Herbig Ae/Be stars in our sample. Circles indicate ground-based near and mid-infrared flux densities obtained from Hillenbrand et al. (1992). Open squares indicate color-corrected *IRAS* flux densities (see text). Ground-based or *IRAS* flux densities have been connected with solid lines to connect their association. Filled triangles indicate flux densities obtained from 2D maps in this paper.

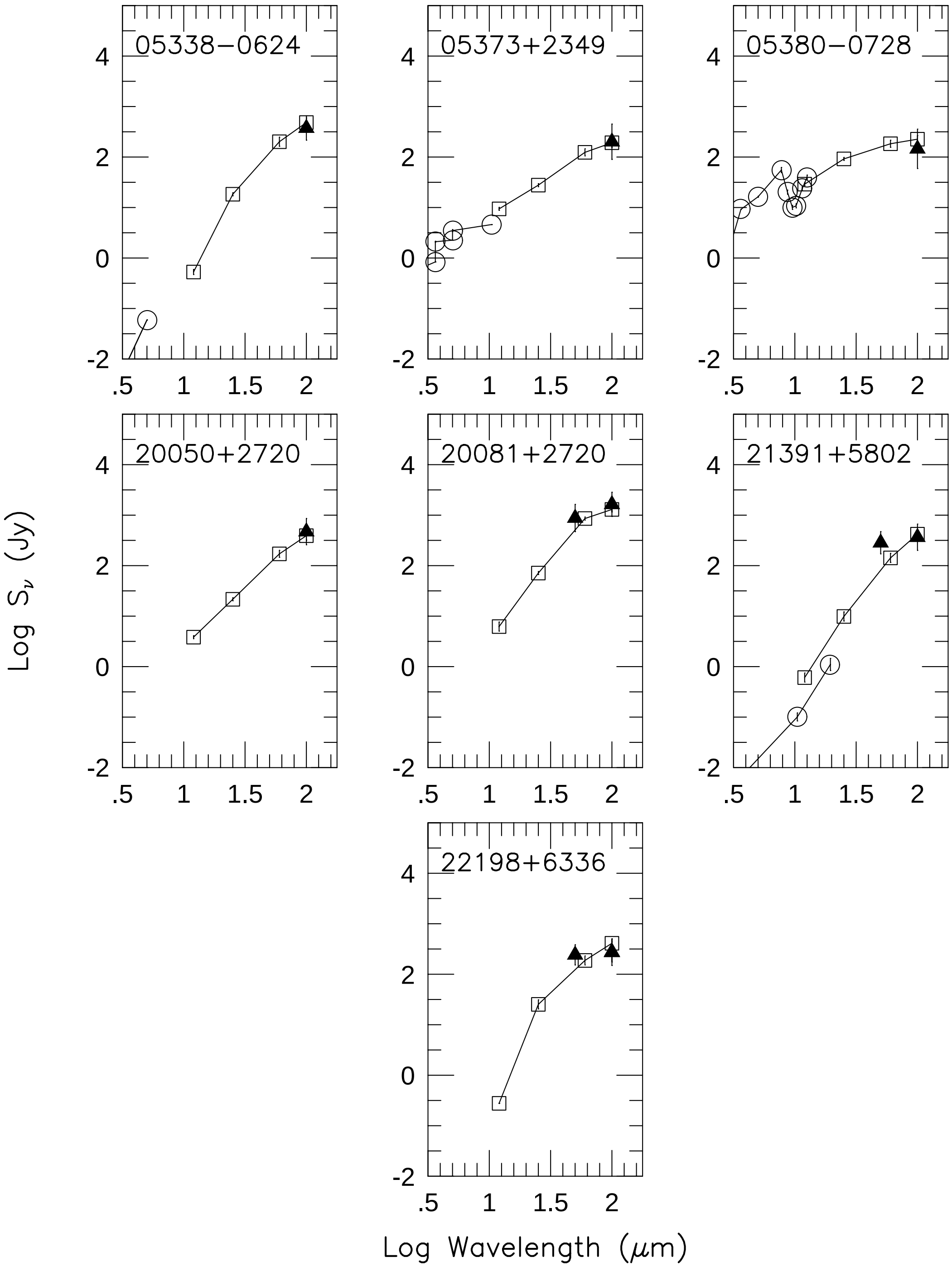

FIG. 24.—Infrared spectral energy distributions for selected embedded *IRAS* objects in our sample. Symbols and lines are defined as for Fig. 23.

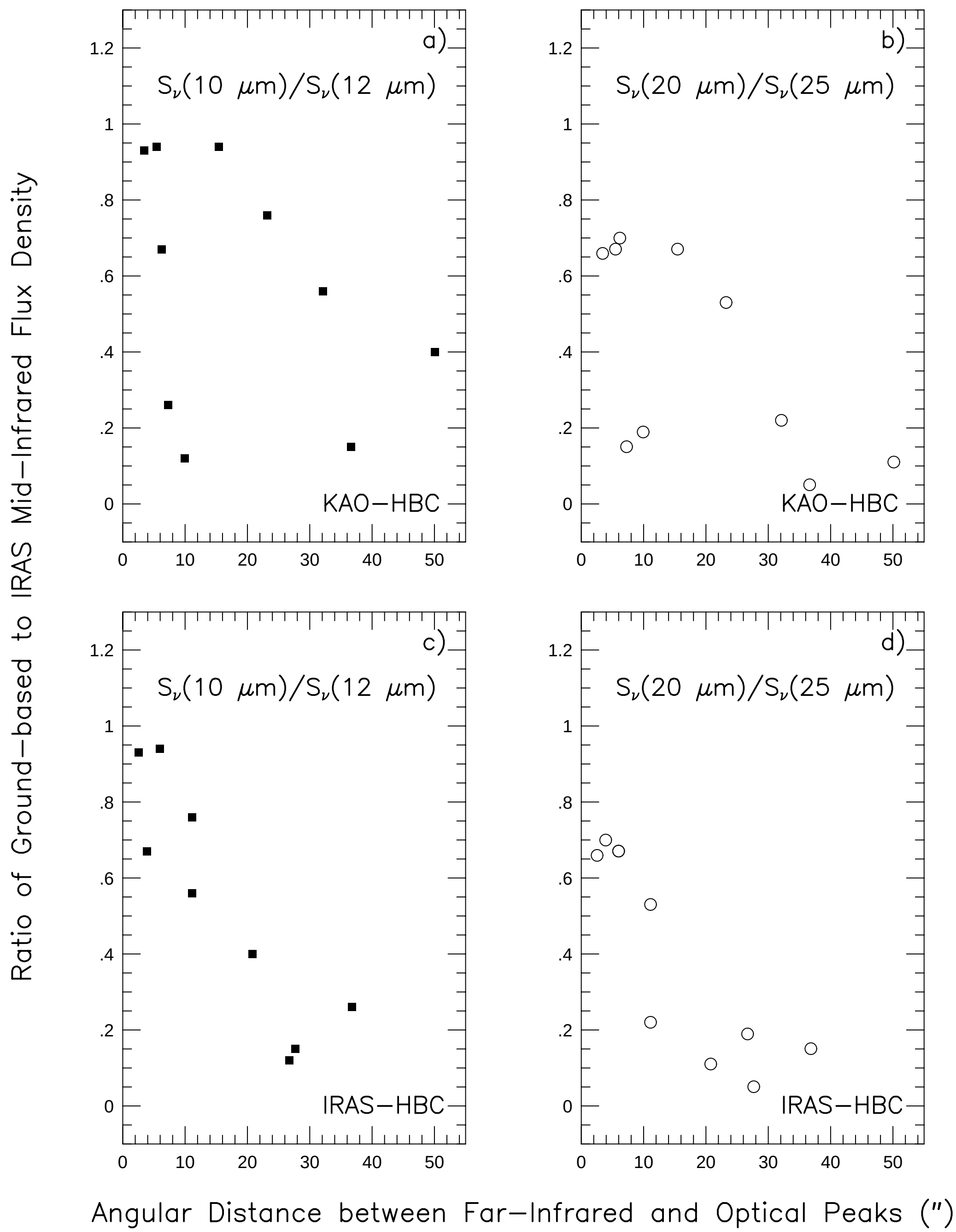

FIG. 25.—Ratios of ground-based mid-infrared photometry to *IRAS* mid-infrared photometry vs. angular distance between KAO peak infrared position and optical position (KAO-HBC; panels *a* and *b*) or between *IRAS* position and optical position (*IRAS*-HBC; panels *c* and *d*) for regions containing Herbig Ae/Be stars in our sample. Ratios were taken between $S_\nu(10\ \mu m)$ and $S_\nu(12\ \mu m)$ (panels *a* and *c*) or between $S_\nu(20\ \mu m)$ and $S_\nu(25\ \mu m)$ (panels *b* and *d*).

TABLE 5

DECONVOLVED SIZES AND SHAPES OF FAR-INFRARED SOURCES

Source Name	λ (μm)	Scan Type	Deconvolved Size (pc)	Aspect Ratio
Elias 3-1	100	2D	$(0.065 \pm 0.0064) \times (0.024 \pm 0.0097)$	2.72 ± 1.13
	100	1D	(0.012 ± 0.0044)	...
AB Aur	100	2D	<0.025	...
	50	2D	<0.019	...
	100	1D	<0.018	...
MWC 137	100	2D	$(0.42 \pm 0.031) \times (0.38 \pm 0.066)$	1.12 ± 0.21
	100	1D	(0.39 ± 0.016)	...
	50	1D	(0.48 ± 0.022)	...
LkHα 215	100	2D	$(0.33 \pm 0.11) \times (0.25 \pm 0.095)$	1.30 ± 0.66
	100	1D	(0.28 ± 0.038)	...
MWC 297	100	2D	$(0.12 \pm 0.021) \times (0.11 \pm 0.027)$	1.09 ± 0.33
	50	2D	$(0.10 \pm 0.024) \times (0.088 \pm 0.029)$	1.19 ± 0.49
	100	1D	(0.13 ± 0.015)	...
	50	1D	(0.11 ± 0.0096)	...
BD+40 4124	100	2D	$(0.17 \pm 0.020) \times (0.13 \pm 0.033)$	1.25 ± 0.35
	50	2D	$(0.26 \pm 0.084) \times (0.20 \pm 0.065)$	1.28 ± 0.59
HD 200775	100	2D	$(0.23 \pm 0.019) \times (0.15 \pm 0.014)$	1.57 ± 0.20
LkHa 234	100	2D	$(0.16 \pm 0.020) \times (0.14 \pm 0.037)$	1.11 ± 0.32
	50	2D	$(0.13 \pm 0.026) \times (0.092 \pm 0.026)$	1.43 ± 0.50
	100	1D	(0.20 ± 0.038)	...
	50	1D	(0.17 ± 0.045)	...
MWC 1080	100	2D	$(0.40 \pm 0.024) \times (0.30 \pm 0.048)$	1.34 ± 0.23
	50	2D	$(0.38 \pm 0.069) \times (0.30 \pm 0.061)$	1.28 ± 0.35
	100	1D	(0.35 ± 0.045)	...
05338−0624	100	2D	$(0.063 \pm 0.0099) \times (0.043 \pm 0.0066)$	1.48 ± 0.33
	100	1D	(0.025 ± 0.018)	...
	50	1D	(0.034 ± 0.021)	...
06249−1007	100	1D	(0.091 ± 0.0089)	...
05373+2349	100	2D	$(0.23 \pm 0.0073) \times (0.075 \pm 0.0056)$	3.05 ± 0.25
05380−0728	100	2D	$(0.066 \pm 0.0067) \times (0.039 \pm 0.0080)$	1.70 ± 0.39
20050+2720	100	2D	$(0.12 \pm 0.0071) \times (0.10 \pm 0.0067)$	1.16 ± 0.10
	100	1D	(0.080 ± 0.014)	...
	50	1D	(0.090 ± 0.019)	...
20081+2720	100	2D	$(0.28 \pm 0.018) \times (0.20 \pm 0.026)$	1.37 ± 0.20
	50	2D	$(0.24 \pm 0.027) \times (0.16 \pm 0.033)$	1.52 ± 0.36
21391+5802	100	2D	$(0.13 \pm 0.010) \times (0.12 \pm 0.013)$	1.06 ± 0.14
	50	2D	$(0.15 \pm 0.012) \times (0.13 \pm 0.029)$	1.15 ± 0.27
	100	1D	(0.086 ± 0.011)	...
21526+5728	100	1D	(0.20 ± 0.021)	...
	50	1D	(0.078 ± 0.015)	...
22198+6336	100	2D	$(0.14 \pm 0.0079) \times (0.12 \pm 0.010)$	1.19 ± 0.12
	50	2D	$(0.11 \pm 0.0093) \times (0.080 \pm 0.014)$	1.36 ± 0.26
	100	1D	(0.088 ± 0.021)	...
23568+6706	100	1D	(0.34 ± 0.055)	...

REFERENCES

Aspin, C., Sandell, G., & Weintraub, D. A. 1994, A&A, 282, L25

Beichmann, C. A. 1985, *Infrared Astronomical Satellite* (*IRAS*) Catalogs and Atlases: Explanatory Supplement (Pasadena: Jet Propulsion Laboratory)

Bevington, P. R. 1969, Data Reduction and Error Analysis for the Physical Sciences (McGraw-Hill: New York)

Butner, H. M., Evans, N. J., II, Lester, D. F., Levreault, R. M., & Strom, S. E. 1991, ApJ, 376, 636

Butner, H. M., & Natta, A. 1995, ApJ, 440, 874

Chen, H., Tafalla, M., Greene, T. P., Myers, P. C., & Wilner, D. J. 1997, ApJ, 475, 163

Colomé, C., Di Francesco, J., & Harvey, P. M. 1996, ApJ, 461, 909

Di Francesco, J., Evans, N. J., II, Harvey, P. M., Mundy, L. G., & Butner, H. M. 1994, ApJ, 432, 710

Di Francesco, J., Evans, N. J., II, Harvey, P. M., Mundy, L. G., Guilloteau, S., & Chandler, C. J. 1997, ApJ, 482, 433

Elias, J. H. 1978, ApJ, 224, 857

Fuller, G. A., & Myers, P. C. 1992, ApJ, 384, 523

Harvey, P. M. 1979, PASP, 91, 143

Harvey, P. M., Lester, D. F., Brock, D., & Joy, M. 1991, ApJ, 368, 558

Herbig, G. H. 1960, ApJS, 4, 337

Hillenbrand, L. A., Meyer, M. R., Strom, S. E., & Strutskie, M. F. 1995, AJ, 109, 280

Hillenbrand, L. A., Strom, S. E., Vrba, F. J., & Keene, J. 1992, ApJ, 397, 613

Kenyon, S. J., Calvet, N., & Hartmann, L. 1993, ApJ, 414, 676

Mannings, V. G., & Sargent, A. I. 1997, ApJ, 490, 792

Myers, P. C., & Fuller, G. A. 1992, ApJ, 396, 631

Myers, P. C., Ladd, E. E., & Fuller, G. A. 1991, ApJ, 372, L95

Natta, A., Palla, F., Butner, H. M., Evans, N. J., II, & Harvey, P. M. 1992, ApJ, 391, 805

———. 1993, ApJ, 406, 674

Press, W. H., Flannery, B. P., Teukolsky, S. A., & Vettering, W. T. 1988, Numerical References in C (Cambridge: Cambridge Univ. Press), 85

Shu, F., Najita, J., Galli, D., Ostriker, E., & Lizano, S. 1993, in Protostars and Planets III, ed. E. H. Levy, J. Lunine, & M. S. Matthews (Tucson: Univ. of Arizona Press), 3

Tedesco, E. F., Veeder, G. J., Fowler, J. W., & Chillemi, J. R. 1992, in *IRAS* Minor Planet Survey (Phillips Laboratory Technical Report PL-TR-92-2049), Hanscom Air Force Base, MA

Testi, L., Palla, F., & Natta, A. 1998, A&AS, in press

Testi, L., Palla, F., Prusti, T., Natta, A., & Maltagliati, S. 1997, A&A, 320, 159

Thé, P. S., de Winter, D., & Pérez, M. R. 1994, A&AS, 104, 315

Whitcomb, S. E., Gatley, I., Hildebrand, R. H., Keene, J., Sellgren, K., & Werner, M. W. 1981, ApJ, 246, 416

Wilking, B. A., Mundy, L. G., Blackwell, J. H., & Howe, J. E. 1989, ApJ, 345, 257 (W89)